Fluctuations in Inner-Core Structure during the Rapid Intensification of Super Typhoon Nepartak (2016)

SAM HARDY,[a] JULIANE SCHWENDIKE,[a] ROGER K. SMITH,[b] CHRIS J. SHORT,[c] MICHAEL J. REEDER,[d,e] AND CATHRYN E. BIRCH[a]

[a] *Institute for Climate and Atmospheric Science, School of Earth and Environment, University of Leeds, Leeds, United Kingdom*
[b] *Meteorologisches Institut, Ludwig-Maximilians Universität, Munich, Germany*
[c] *Met Office, Exeter, United Kingdom*
[d] *School of Earth, Atmosphere and Environment, Monash University, Melbourne, Victoria, Australia*
[e] *ARC Centre of Excellence for Climate Extremes, Monash University, Melbourne, Victoria, Australia*

ABSTRACT: The key physical processes responsible for inner-core structural changes and associated fluctuations in the intensification rate for a recent, high-impact western North Pacific tropical cyclone that underwent rapid intensification [Nepartak (2016)] are investigated using a set of convection-permitting ensemble simulations. Fluctuations in the inner-core structure between ringlike and monopole states develop in 60% of simulations. A tangential momentum budget analysis of a single fluctuation reveals that during the ringlike phase, the tangential wind generally intensifies, whereas during the monopole phase, the tangential wind remains mostly constant. In both phases, the mean advection terms spin up the tangential wind in the boundary layer, whereas the eddy advection terms deepen the storm's cyclonic circulation by spinning up the tangential wind between 1.5 and 4 km. Calculations of the azimuthally averaged, radially integrated vertical mass flux suggest that periods of near-constant tangential wind tendency are accompanied by a weaker eyewall updraft, which is unable to evacuate all the mass converging in the boundary layer. Composite analyses calculated from 18 simulations produce qualitatively similar results to those from the single case, a finding that is also in agreement with some previous observational and modeling studies. Above the boundary layer, the integrated contribution of the eddy term to the tangential wind tendency is over 80% of the contribution from the mean term, irrespective of inner-core structure. Our results strongly indicate that to fully understand the storm's three-dimensional evolution, the contribution of the eddies must be quantified.

KEYWORDS: Convective-scale processes; Hurricanes/typhoons; Budgets; Tropical cyclones; Ensembles

1. Introduction

The vast majority of the most intense and destructive tropical cyclones across all ocean basins undergo rapid intensification (e.g., Wang and Zhou 2008; Shu et al. 2012; Lee et al. 2016). Rapid intensification (RI) is defined as the 95th percentile of all 24-h intensity changes for storms over the ocean, which equates to values greater than $15\,\mathrm{m\,s}^{-1}\,(24\,\mathrm{h})^{-1}$ (Kaplan and DeMaria 2003; Kaplan et al. 2010). Accurately forecasting the timing and magnitude of RI remains one of the most difficult challenges in modern-day meteorology, with little notable improvement in operational intensity forecasts in the past 30 years, especially at shorter lead times (e.g., DeMaria et al. 2014; National Oceanic and Atmospheric Administration 2017). The difficulty in accurately forecasting the timing and magnitude of RI stems partly from its multiscale nature, with interacting processes over scales ranging from the environmental scale, through the vortex scale, and down to the microscale (e.g., Kaplan et al. 2010), and partly from an incomplete knowledge of the key physical processes themselves (e.g., Rogers et al. 2013).

On the scale of the storm's inner core, structural changes can strongly influence the intensification rate. In the case of eyewall replacement cycles, when the entire primary eyewall of a strong, mature tropical cyclone weakens and is replaced by a contracting outer or secondary eyewall, these changes can be dramatic and result in pronounced intensity fluctuations (e.g., Willoughby et al. 1982; Sitkowski et al. 2011; Abarca and Montgomery 2013). In other situations, structural changes can be more subtle, as with vortex Rossby waves (e.g., Guinn and Schubert 1993; Montgomery and Kallenbach 1997) where the storm's mean negative radial potential vorticity gradient supports outward-propagating vortex Rossby waves analogous to planetary-scale Rossby waves in the midlatitudes (Macdonald 1968). More fundamentally, the towering ring of enhanced, diabatically generated eyewall potential vorticity can become barotropically unstable and break down into either discrete mesovortices or a monopolar vorticity structure (e.g., Schubert et al. 1999; Rozoff et al. 2006, 2009). This instability mechanism mixes vorticity, momentum and high-entropy air between the eye and eyewall, which can have a pronounced impact on the radial profiles of inner-core inertial stability and momentum (e.g., Kossin and Schubert 2001; Cram et al. 2007; Hendricks and Schubert 2010; Hendricks et al. 2012, 2014).

Structural characteristics of the inner core most favorable for intensification were identified by Kossin and Eastin (2001), who constructed radial profiles of angular velocity and relative vorticity using aircraft data from a 20-yr dataset of Atlantic and eastern North Pacific tropical cyclones. They demonstrated

---

Corresponding author: Sam Hardy, s.hardy1@leeds.ac.uk

that the highest rates of intensification occurred when the inner core had a ringlike structure with high values of relative vorticity in the eyewall surrounding lower values in the eye (termed regime 1). Conversely, intensification rates were much lower when the relative vorticity profile was largely monotonic (their regime 2). Similar results were documented for Hurricanes Olivia (1994; Reasor et al. 2000), Elena (1985; Corbosiero et al. 2005, 2006) and Guillermo (1997; Reasor et al. 2009), and in the composite study by Rogers et al. (2013), suggesting that this relationship between inner-core structure and the intensification rate could be widely representative of developing tropical cyclones in other ocean basins.

Despite the robust body of observational evidence supporting the relationship between tropical cyclone inner-core structure and intensification rate, numerical modeling studies have been few, with only a single hurricane [Katrina (2005)] analyzed in detail (Nguyen et al. 2011; Hankinson et al. 2014; Reif et al. 2014). Nguyen et al. (2011) and Hankinson et al. (2014) both ran convection-permitting (0.05° horizontal grid spacing), hydrostatic simulations of Katrina's intensification using the Australian Bureau of Meteorology's Tropical Cyclone Limited Area Prediction System model. In their analysis of a single simulation, Nguyen et al. (2011) showed that Katrina's inner core fluctuated between symmetric (ringlike) and asymmetric (monopole) states, and that the strongest increases in low-level wind speed occurred preferentially during the ringlike phase, in agreement with the results from earlier observational studies.

During the ringlike phase, the wind speed strengthened near the radius of maximum mean tangential wind whereas during the monopole phase, mixing of vorticity and high-entropy air between the eye and the eyewall increased the wind speed in the eye, but weakened the flow near the radius of maximum wind. Nguyen et al. (2011) hypothesized that a combination of barotropic and convective instabilities could be driving the ringlike to monopole transition. In contrast, Nguyen et al. (2011) suggested that the monopole to ringlike transition was preceded by the development of convection beyond the radius of maximum wind, in a region of enhanced convective instability, which subsequently moved inward in a similar manner to the secondary eyewall during an eyewall replacement cycle. Nguyen et al. (2011) termed these fluctuations between ringlike and monopole states vacillation cycles. Hankinson et al. (2014) tested the sensitivity of the simulated vortex to changes in several parameters, including the sea surface temperature (SST), using a 22-member ensemble. A large number (77%) of their simulations produced vacillation cycles, with development favored over higher SSTs and for vortices characterized by a reversal in sign of the radial vorticity gradient, further suggesting that a combination of convective and barotropic instabilities could be driving the ringlike to monopole transition.

The foregoing results suggest that to fully understand the relationship between intensification and inner-core structure, the role played by localized deep convection in the inner core on the three-dimensional evolution of the vortex must be quantified (see discussion of the rotating convection paradigm in Montgomery and Smith 2014, 2017; Zhu and Smith 2020). In the rotating convection paradigm, convective updrafts locally amplify the vorticity by vortex-tube stretching, and these patches of enhanced vorticity eventually aggregate to form a central vorticity monopole (Montgomery and Smith 2017). As such, the paradigm builds on the classical intensification mechanism of Ooyama (1969), in part by incorporating the collective effects of asymmetric processes on the spinup of the maximum tangential wind in the vortex. Given the growing support for the rotating convection paradigm and the robust observational evidence for a relationship between inner-core structure and intensification rate, the purpose of this paper is to test the validity of the paradigm for a recent, high-impact western North Pacific Super Typhoon that underwent fluctuations in its intensification rate [Nepartak (2016)]. Convection-permitting ensemble simulations and tangential momentum budget analyses will be used to quantify the respective roles of axisymmetric and asymmetric processes during intensification.

The remainder of the article is structured as follows. Section 2 introduces the numerical model used for the convection-permitting ensemble simulations, alongside the tangential momentum budget equation and the method used to characterize the storm's inner-core structure. In section 3, a brief synoptic overview of Nepartak is presented, before the ensemble simulations are summarized. Section 4 identifies the contributions of axisymmetric and asymmetric processes during periods of differing intensification rate during Nepartak's RI for a single simulation, before composite analyses are developed using data from multiple simulations. The relationship between the likelihood of inner-core fluctuations and both mesoscale and convective-scale processes is discussed in section 5, and the conclusions are given in section 6.

2. Data and methods

a. Numerical model

A limited-area configuration of the Met Office Unified Model (MetUM; Cullen 1993) has been used to produce convection-permitting ensemble forecasts for Typhoon Nepartak. The MetUM solves the full, deep-atmosphere, nonhydrostatic equations of motion using a semi-implicit, semi-Lagrangian numerical scheme (see Wood et al. (2014) for details). Model prognostic variables are discretized on to a grid with Arakawa C grid staggering (Arakawa and Lamb 1977) in the horizontal and Charney–Phillips grid staggering (Charney and Phillips 1953) in the vertical, with a hybrid height–terrain-following vertical coordinate.

The science configuration of the MetUM used in the ensemble is the tropical version of the Regional Atmosphere and Land 1 (RAL1) configuration presented in Bush et al. (2020) (known as RAL1-T), but with reduced air–sea drag at high wind speeds, as motivated by observational data (Powell et al. 2003; Black et al. 2007). This single change has been shown to improve the match to the observed wind–pressure relation of tropical cyclones and will be included in RAL2-T. Note that RAL1-T does not include a source term in the boundary layer scheme representing heating from the dissipation of turbulence, known to generate more intense storms in numerical models (Zhang and Altshuler 1999; Jin et al. 2014).
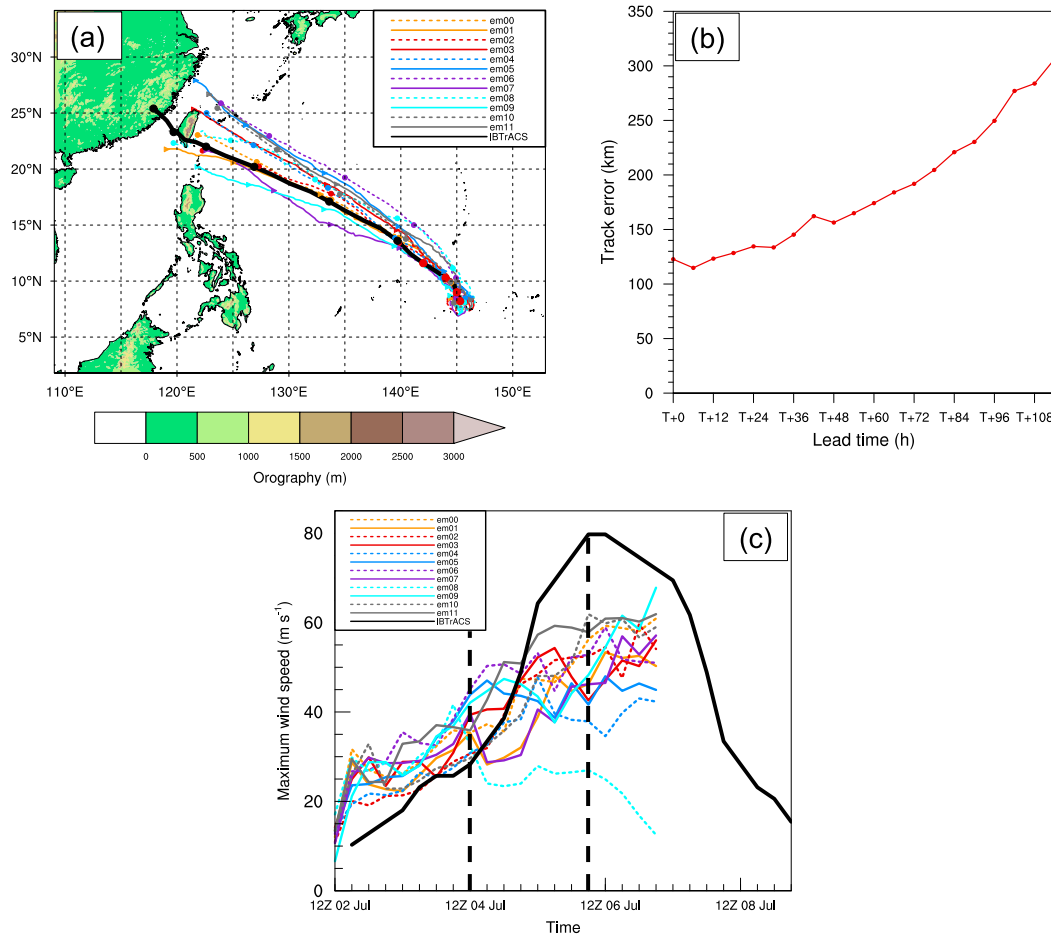
FIG. 1. (a) Regional model domain and orography. The black line shows the International Best Track Archive for Climate Stewardship (IBTrACS) observed track of Typhoon Nepartak (2016) with the red circles showing the position of the storm at the initialization times of the four forecasts analyzed in this study: 1200 UTC 2 Jul, 0000 UTC 3 Jul, 1200 UTC 3 Jul, and 0000 UTC 4 Jul 2016, and the black circles showing the position of the storm every 24 h between 1200 UTC 4 Jul and 1200 UTC 9 Jul 2016. The 12 RAL1-T ensemble forecasts initialized at 1200 UTC 2 Jul 2016 are overlaid according to the legend, with the corresponding markers denoting the storm position every 24 h from $T + 0$ to $T + 120$. (b) Mean track error (km) as a function of forecast lead time, where the mean is taken across all members and all forecasts. (c) Comparison of the maximum 10 m wind speed of Typhoon Nepartak (2016) between the IBTrACS best track data (thick black line) and the 12 RAL1-T ensemble forecasts initialized at 1200 UTC 2 Jul 2016 (thin lines). Overlaid are the start and end times of Nepartak's rapid intensification from the IBTrACS dataset (black dashed lines).

The regional model domain consists of 1098 and 810 grid points in the zonal and meridional directions, respectively, with a grid spacing of 0.04° (about 4.4 km) in both directions (Fig. 1a). The domain has been constructed so that Nepartak is located well inside the lateral boundary at the initialization time of each forecast. In the vertical direction there are 80 levels, the spacing of which increases quadratically with height, relaxing toward a horizontal lid 38.5 km above sea level. The model time step is 75 s.

Each member of the ensemble is one-way nested inside a corresponding member of the Met Office global ensemble prediction system, MOGREPS-G (Bowler et al. 2008). The science configuration of the MetUM used in MOGREPS-G is known as Global Atmosphere 6.1 (GA6.1; Walters et al. 2017),

which is currently used operationally at the Met Office for global numerical weather prediction. The global model grid spacings are 0.45° and 0.3° in the zonal and meridional directions (about 50 km × 33 km in the tropics), corresponding to 800 and 600 grid points, respectively. In the vertical there are 70 levels up to a fixed model lid 80 km above sea level. The model time step is 12 min.

Initial conditions for each MOGREPS-G member are formed by adding perturbations to the Met Office global analysis, where the perturbations are generated using an ensemble transform Kalman filter (Bishop et al. 2001). MOGREPS-G also includes two stochastic physics schemes to represent the effects of structural and subgrid-scale model uncertainties: the random parameters scheme (Bowler et al. 2008)

and the stochastic kinetic energy backscatter scheme (Bowler et al. 2009). The initial state of each MOGREPS-G member is interpolated to the finer regional grid to generate initial conditions for the nested convection-permitting ensemble members. In other words, there is no data assimilation or vortex specification scheme in the regional model itself, but central pressure estimates from tropical cyclone warning centers are assimilated as part of the global data assimilation cycle (Heming 2016). Lateral boundary conditions for each convection-permitting member are provided by the driving MOGREPS-G member at an hourly frequency. The initial SSTs, which differ between perturbed members, are held fixed throughout each forecast. No stochastic physics schemes are included in the convection-permitting ensemble, so that ensemble spread is purely the result of differences in initial and boundary conditions inherited from the driving model. In total, four 12-member convection-permitting ensemble forecasts were produced for Nepartak, initialized every 12 h between 1200 coordinated universal time (UTC) 2 July 2016 and 0000 UTC 4 July 2016. All forecasts were run out to 5 days, and in all analyses, the model spinup period (0 to 24 h into the forecast; hereafter, given in the form $T + 0$ to $T + 24$) has been discarded.

b. Budget analysis

TANGENTIAL MOMENTUM EQUATION

To identify the key processes responsible for changes in the swirling flow around the storm, the storm-relative azimuthally averaged tangential momentum equation is analyzed using a similar method to Persing et al. (2013). First, the storm center is identified on each model level using the minimum wind speed within 0.15° of the minimum pressure on that model level.[1] Then, all variables are interpolated onto a cylindrical grid centered on the local storm center, and decomposed into azimuthally averaged (mean) and asymmetric (eddy) components, defined by the overbar and prime symbols, respectively. The eddy component represents the departure from the mean at each grid point. The rate of change of the azimuthally averaged tangential wind is

$$\frac{\partial \overline{v}}{\partial t} = \underbrace{-\overline{u}(\overline{\zeta} + f)}_{V_{m\zeta}} - \underbrace{\overline{w}\frac{\partial \overline{v}}{\partial z}}_{V_{mv}} - \underbrace{\overline{u'\zeta'}}_{V_{e\zeta}} - \underbrace{\overline{w'\frac{\partial v'}{\partial z}}}_{V_{ev}} + \underbrace{\overline{F_{\lambda}}}_{V_d}, \quad (1)$$

where t is time, u, v, and w are the radial, tangential and vertical velocity components, respectively; ζ is the vertical component of relative vorticity; and f is the Coriolis parameter. In Eq. (1), the left-hand side represents the local mean tangential wind tendency, and the right-hand-side terms represent the mean radial vorticity flux ($V_{m\zeta}$), the mean vertical advection of mean tangential momentum (V_{mv}), the eddy radial vorticity flux

($V_{e\zeta}$), the vertical advection of eddy tangential momentum (V_{ev}), and the combined horizontal and vertical diffusive tendency of tangential momentum (V_d). As a consequence of the partitioning method, localized asymmetric features project onto both the mean and eddy terms. For example, a vertical velocity maximum will project onto both V_{mv} and V_{ev} in Eq. (1). The horizontal (F_h) and vertical (F_v) components of V_d are calculated on the model's Cartesian grid following the method of Persing et al. (2013):

$$F_{xh} = \frac{\partial \tau_{xx}}{\partial x} + \frac{\partial \tau_{xy}}{\partial y},$$

$$F_{yh} = \frac{\partial \tau_{xy}}{\partial x} + \frac{\partial \tau_{yy}}{\partial y},$$

$$F_{xv} = \frac{\partial \tau_{xz}}{\partial z},$$

$$F_{yv} = \frac{\partial \tau_{yz}}{\partial z}. \quad (2)$$

These expressions are subsequently transformed into cylindrical coordinates. The turbulent stress tensor components are expressed in the following form (Kundu and Cohen 2002, p. 561), where ρ is the dry air density and ν_h and ν_v are the horizontal and vertical eddy viscosities, respectively:

$$\tau_{xz} = \rho\nu_v\frac{\partial u}{\partial z} + \rho\nu_h\frac{\partial w}{\partial x},$$

$$\tau_{yz} = \rho\nu_v\frac{\partial v}{\partial z} + \rho\nu_h\frac{\partial w}{\partial y},$$

$$\tau_{xy} = \rho\nu_h\left(\frac{\partial u}{\partial y} + \frac{\partial v}{\partial x}\right),$$

$$\tau_{xx} = 2\rho\nu_h\frac{\partial u}{\partial x},$$

$$\tau_{yy} = 2\rho\nu_h\frac{\partial v}{\partial y}. \quad (3)$$

The azimuthally averaged pressure gradient term [e.g., Persing et al. 2013, their Eq. (12)] is several orders of magnitude smaller than the other terms, and has been neglected. For the analysis of a single simulation in sections 4a and 4b, data with an output frequency of 5 min are used, whereas the composite analysis in section 4c is based on data output every 1 h.

c. Characterizing inner-core structure

Once the storm center has been identified on each model level using the method described above, the inner-core structure is characterized as follows:

- On each model level, a cylindrical grid is constructed about the storm center identified on this level, using 5 km radial bands out to a radius of 50 km. The relative vorticity field is interpolated on to this cylindrical grid, and the azimuthal and 1–4 km layer average is computed.
- At each time, the ratio of the relative vorticity at the storm center, ζ_0, and that at the radius of maximum vorticity, ζ_x [hereafter, the vorticity ratio $(\zeta_0/\zeta_x) = R$] is computed. For a monopolar inner core with maximum vorticity at its center,

---

[1] This method, which effectively removes the vortex center tilt, was chosen because it improved the accuracy of the budget calculation. The maximum horizontal displacement between the local center at the surface and that on any other model level is 0.19°.

Ring-like
1815 UTC 4 July

Monopole
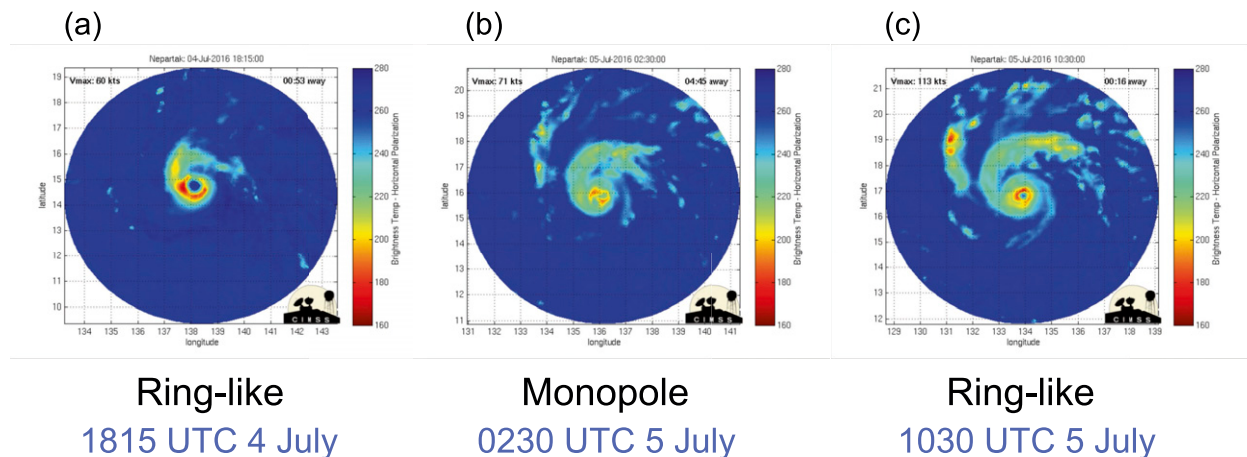### 0230 UTC 5 July

Ring-like
1030 UTC 5 July

FIG. 2. Plots of brightness temperature (shaded, K) from the Morphed Integrated Microwave Imagery at CIMSS (MIMIC) product for Typhoon Nepartak (2016), output every 15 min: (a) 1815 UTC 4 Jul, (b) 0230 UTC 5 Jul, and (c) 1030 UTC 5 Jul 2016. Source: http://tropic.ssec.wisc.edu/real-time/mimic-TC/2016_02W/webManager/mainpage.html.

$R = 1$, whereas for a ringlike inner core with maximum vorticity some distance from the center, $R < 1$.

- A three-point running average is applied to the time series of R, and four phases are defined:
  1) Ringlike phase: local minima of R;
  2) Ringlike to monopole transition: $\partial R/\partial t$ greater than 0;
  3) Monopole phase: $R = 1$;
  4) Monopole to ringlike transition: $\partial R/\partial t$ less than 0.

The ringlike and monopole phases correspond to regimes 1 and 2 from the observational study of Kossin and Eastin (2001), respectively. Their analysis of Hurricane Olivia (1994) showed that transitions between regimes can occur in less than 1 h. In the analysis herein, fluctuations with periods > 24 h are ignored, which excludes lower-frequency eyewall replacement cycles.

3. Super Typhoon Nepartak (2016)

a. Synoptic overview

Nepartak was a high-impact and deadly storm, directly responsible for 108 fatalities and economic losses of over $1.85 billion (U.S. dollars) (World Meteorological Organization 2017). Nepartak first developed as a tropical depression close to Guam on 2 July 2016, before strengthening to a tropical storm on 3 July 2016 as it moved west-northwestward around the southern flank of an extensive subtropical ridge. In favorable environmental conditions defined by SSTs $\geq 30°C$ and 200–850 hPa shear $\leq 5 \text{ m s}^{-1}$, Nepartak rapidly intensified to become a category 5 tropical cyclone between 1200 UTC 4 July and 0600 UTC 6 July as it continued its northwestward track, with maximum 10 m wind speed increasing from 28 to 80 m s^{-1} and minimum mean sea level pressure falling from 985 to 907 hPa over the same period (Fig. 1c). This period of intensification included a 24-h increase in wind speed of 36 m s^{-1} between 0000 UTC 5 and 6 July, over twice the threshold for RI.

During Nepartak's main period of intensification between 1200 UTC 4 July and 0600 UTC 6 July, plots of brightness temperature from the Morphed Integrated Microwave Imagery at the Cooperative Institute for Meteorological Satellite Studies satellite product (output at 15-min intervals) demonstrate that Nepartak's inner-core structure fluctuated from a ringlike state at 1815 UTC 4 July, with a brightness temperature minimum surrounding a well-defined maximum (Fig. 2a), to a monopolar structure without a central maximum in brightness temperature by 0230 UTC 5 July (Fig. 2b), before the ringlike structure reformed by 1030 UTC 5 July (Fig. 2c). As a caveat, although the ringlike pattern of deep convection in these satellite images suggests enhanced vorticity, it does not guarantee it. Nevertheless, the observations provide evidence of a fluctuation in the inner-core structure from ringlike to monopole and back again. These two observed inner-core states are qualitatively similar to regimes 1 and 2 documented by Kossin and Eastin (2001), and both the structure and timing of the fluctuations are comparable to those in the microwave satellite images of Katrina (2005) presented by Nguyen et al. (2011, their Fig. 5). This observed fluctuation takes about 16 h (cf. Figs. 2a,c), which is comparable to Katrina's 17 h (cf. their Figs. 5d,f), suggesting similarities in the mechanisms driving the fluctuations in both cases.

b. Summary of ensemble forecasts

As discussed in section 3a, Nepartak's main RI period occurred between 1200 UTC 4 July and 0600 UTC 6 July 2016, after which the storm remained a category 5 tropical cyclone until 0000 UTC 8 July 2016. The analysis herein focuses on four 12-member RAL1-T ensemble forecasts initialized at 1200 UTC 2 July 0000 and 1200 UTC 3 July, and 0000 UTC 4 July, respectively, chosen to encompass Nepartak's early development and initial intensification periods as well as the main period of RI.

The RAL1-T ensemble forecast initialized at 1200 UTC 2 July 2016 generally captures Nepartak's observed motion according to the International Best Track Archive for Climate Stewardship (IBTrACS; Knapp et al. 2010) dataset (Fig. 1a). All simulations produced a west-northwestward-moving storm, with a mean track error of about 150 km after 48 h, and 250 km after 96 h (Fig. 1b).
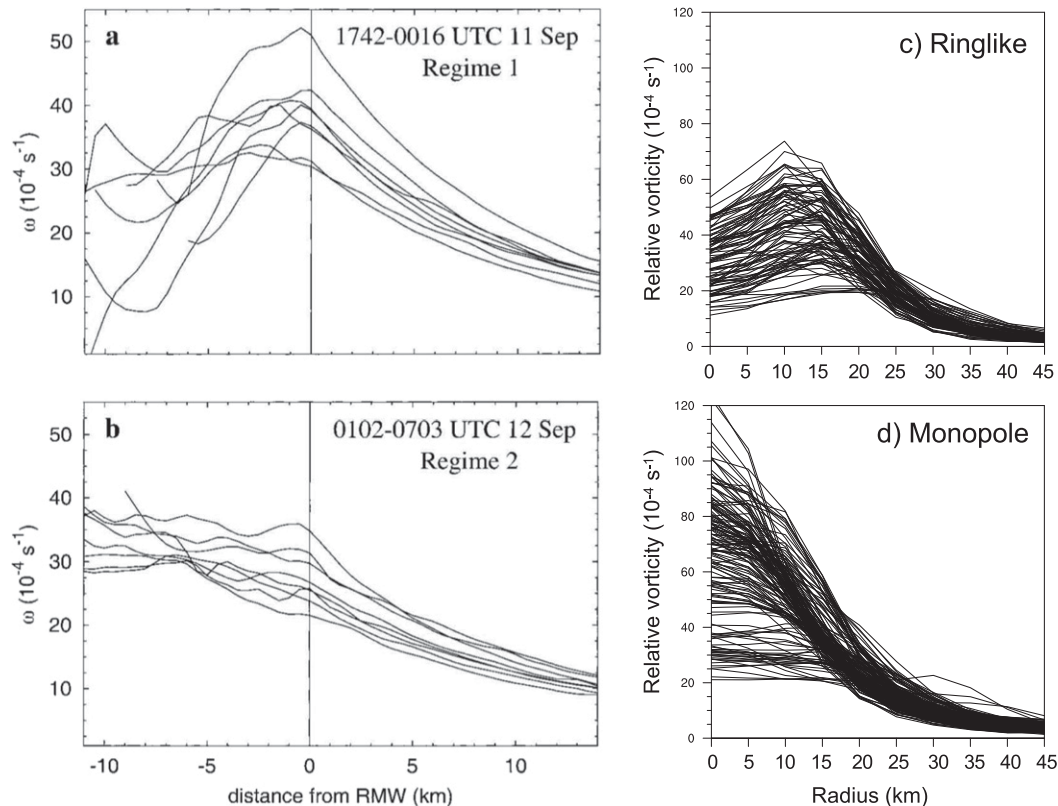
FIG. 3. Radial profiles of angular velocity from observational flight-level data in Hurricane Diana (1984) taken from Kossin and Eastin (2001) for their (a) regime 1 and (b) regime 2. Radial profiles of 1–4 km layer-averaged relative vorticity from 16 Met Office Unified Model simulations of Typhoon Nepartak (2016) for the (c) ringlike and (d) monopole phases.

Although almost all forecasts simulate an intensifying storm, the modeled wind speed does not increase rapidly for 48 h as in the IBTrACS analysis, nor does the model correctly capture the timing of the peak 10 m wind speed (Fig. 1c). These are expected results given the difficulty that even high-resolution numerical models have in reproducing the timing and magnitude of RI (e.g., Short and Petch 2018). Nevertheless, 30 of the 48 total forecasts (63%) simulate a rapidly intensifying storm within 12 h of the occurrence of RI in the IBTrACS dataset (not shown), indicating that the model is able to capture the timing and magnitude of RI reasonably well. Although IBTrACS is a reliable indicator of the occurrence of RI, data are available only every 6 h and thus cannot capture any higher-frequency changes in wind speed associated with inner-core fluctuations, which may occur on time scales of 6 h or less. Generally, however, the performance of the ensemble forecasts relative to IBTrACS gives us confidence to proceed with more detailed analysis of the key physical processes driving the changes in inner-core structure during RI.

4. Results

Inner-core fluctuations are identified following the method outlined in section 2c. This method uses R to define ringlike and monopole inner-core states, motivated by the results of the observational study of Kossin and Eastin (2001). Fluctuations between ringlike and monopolar states develop in 29 of the 48 forecasts (60%), providing sufficient data to calculate composite diagnostics. In section 4c, composite analyses are calculated using hourly data from the 16 simulations with the most pronounced fluctuations, as defined by the magnitude of peak to trough fluctuation in R.

The ringlike and monopole phases in these 16 simulations share similarities with the two regimes identified by Kossin and Eastin (2001) (Fig. 3). During the ringlike phase that corresponds to their regime 1, the relative vorticity peaks at some distance from the eye (cf. Figs. 3a,c), corresponding to values of $R < 1$. Conversely, during the monopole phase, corresponding to their regime 2, the relative vorticity is highest in the eye and decreases radially outward (cf. Figs. 3b,d), which corresponds to values of $R = 1$. During Nepartak's monopole phase, two subsets of radial profile are evident. The first subset is characterized by sharply decreasing relative vorticity outward from the eye, whereas the second is characterized by almost constant relative vorticity between radii of 0 and 15 km and weaker relative vorticity in the eye than the first subset (Fig. 3d). Nevertheless, the overall qualitative similarities between the radial profiles of Nepartak and Diana suggest that the simulated fluctuations are representative of realistic observed changes in tropical cyclone inner-core structure.
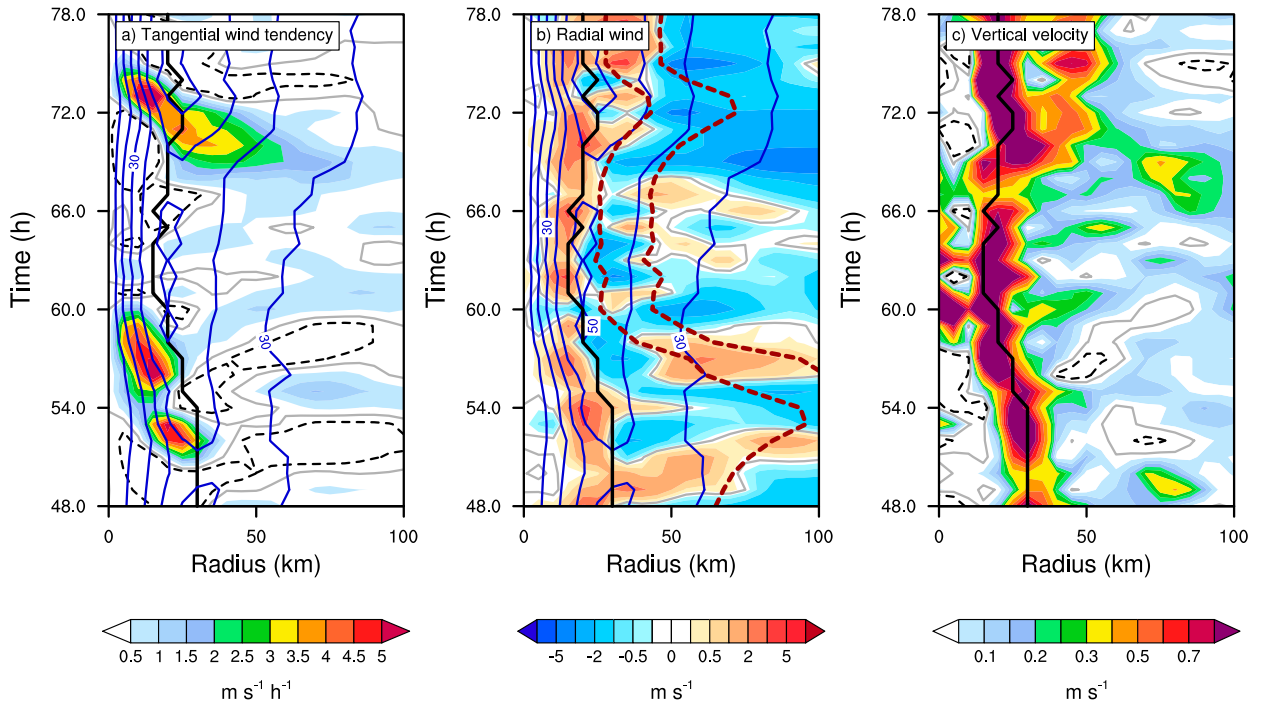
FIG. 4. Hovmöller plot of (a) tangential wind tendency ($m\,s^{-1}\,h^{-1}$), (b) radial wind ($m\,s^{-1}$), and (c) vertical velocity ($m\,s^{-1}$) for simulation em11, initialized at 1200 UTC 2 Jul 2016, between $T + 48$ and $T + 78$. The radius of maximum wind (black contour) is overlaid in all panels, and the mean tangential wind (blue contours, every $10\,m\,s^{-1}$, from $30\,m\,s^{-1}$) is overlaid on (a) and (b). Absolute angular momentum (hereafter M) surfaces (dashed dark red contours; 1.0 and $1.5\,m^2\,s^{-1}$) are overlaid in (b). In (a) and (b), the tangential wind tendency, the radial wind, and M are calculated using a layer average between 1 and 1.5 km, and in (c), the vertical velocity is calculated using a layer average between 1.5 and 4 km.

The contributions of the mean and eddy terms in Eq. (1) to changes in the intensification rate in these 16 simulations are discussed in section 4c. First, the changes in inner-core structure associated with a single fluctuation, which developed in simulation em11 initialized at 1200 UTC 2 July 2016, are investigated in sections 4a and 4b.

a. Inner-core structural changes during a single fluctuation

The inner-core structural changes during this fluctuation are illustrated in a Hovmöller panel plot of layer-averaged tangential wind tendency (Fig. 4a), radial wind (Fig. 4b) and vertical velocity (Fig. 4c) motivated by Fig. 6 in Nguyen et al. (2011). The tangential wind tendency and radial wind are averaged between heights of 1 and 1.5 km. This layer has been chosen to capture any regions of outflow that develop just above the surface-based inflow layer. Although the maximum tangential wind generally occurs below 1 km (see, e.g., Zhang et al. 2011, their Figs. 4 and 5), averaging between 1 and 1.5 km provides a close approximation to its location and strength. Vertical velocity is generally stronger in the low to midtroposphere than nearer the surface, and so is layer averaged between 1.5 and 4 km.

The tangential wind tendency can be split into three main phases, the period of intensification between $T + 51$ and $T + 60$, the near-constant wind speed between $T + 60$ and $T + 69$ and the second period of intensification between $T + 69$ and $T + 75$

(Fig. 4a). Between $T + 51$ and $T + 60$, the eyewall moves inward from a radius of about 35 to 20 km (Fig. 4c), coincident with an increase in the mean tangential wind (Fig. 4a) and associated inward movement of the absolute angular momentum (hereafter M) surfaces (Fig. 4b). This intensification is followed by a period of near-constant wind speed, with the eyewall updraft remaining around 20 km from the local axis of rotation, between $T + 60$ and $T + 69$ (Fig. 4c). These two states share similarities with regimes 1 and 2 described by Kossin and Eastin (2001). The mean tangential wind intensifies once more between $T + 69$ and $T + 75$, coincident with a second inward movement of the eyewall updraft (cf. Figs. 4a,b), indicating that periodic fluctuations in the inner-core structure are occurring in conjunction with changes in the intensification rate.

Between $T + 48$ to $T + 78$, there is often mean inflow immediately outward of the main eyewall updraft (Fig. 4b). This inflow is interspersed with pulses of outflow extending out from the main eyewall updraft region such as at $T + 54$, $T + 60$, and between $T + 65$ and $T + 68$. The small peak in outflow at $T + 54$ is accompanied by a weakening in the mean vertical velocity (cf. Figs. 4b,c), suggesting that the convection at that time is unable to evacuate all the incoming mass converging in the boundary layer. The more pronounced weakening in the vertical velocity at $T + 67$ is accompanied by a pulse of outflow extending out from the eyewall updraft region, suggestive of a
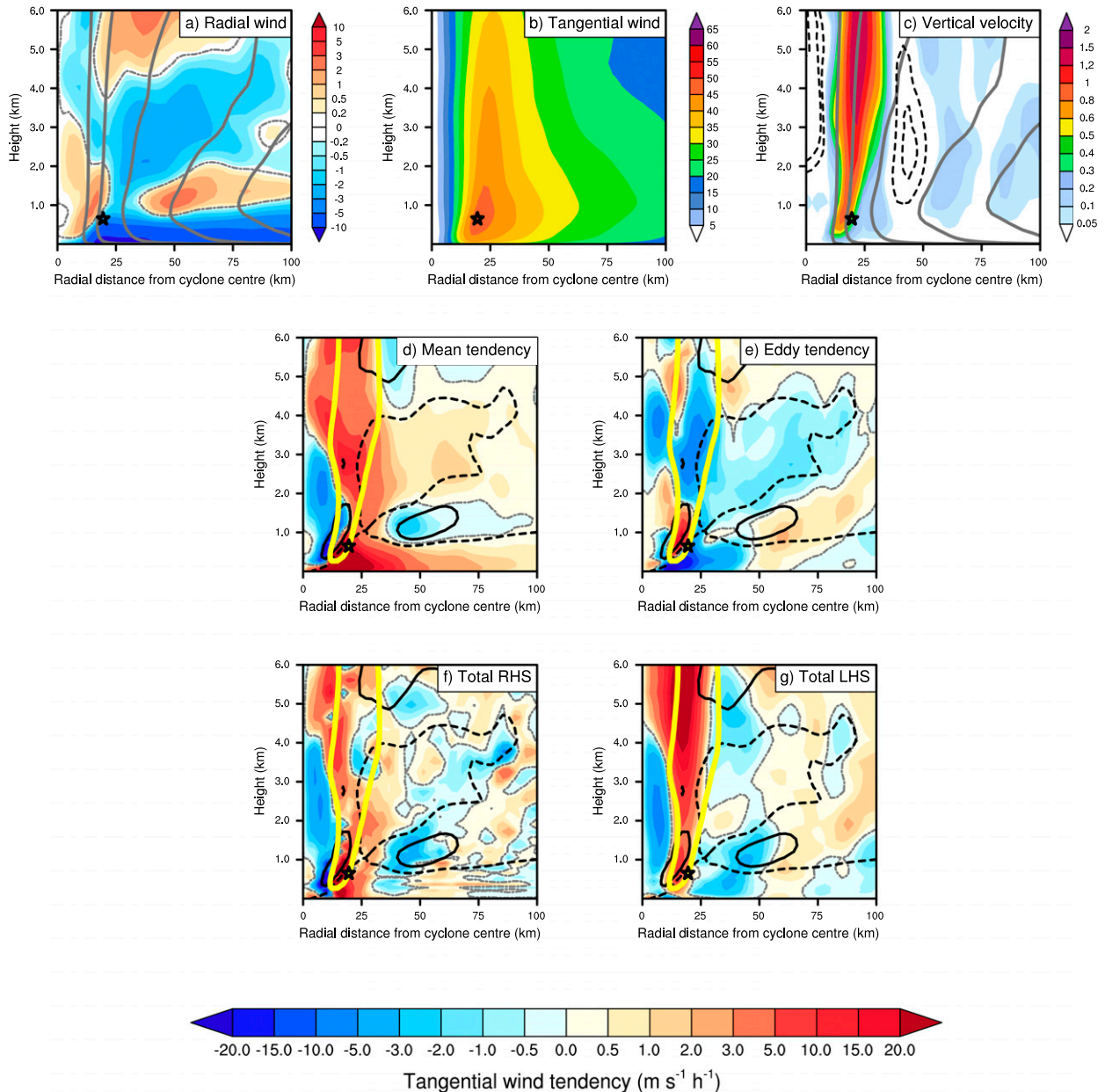
FIG. 5. Radius–height plots at $T + 57$ from simulation em11, initialized at 1200 UTC 2 Jul 2016, using a 5-min output interval. Azimuthally averaged (a) radial wind, (b) tangential wind, and (c) vertical velocity, all shaded according to the color bars with units m s^{-1}, with M surfaces overlaid in (a) and (c) (gray contours; 0.5 to 2.5 m^2 s^{-1}, every 0.5 m^2 s^{-1}). The radial wind zero line (thin gray contour) is overlaid in (a). Azimuthally averaged (d) combined mean radial vorticity flux and mean vertical advection of mean tangential momentum, (e) combined eddy radial vorticity flux and eddy vertical advection of eddy tangential momentum, and (f) sum of all right-hand-side terms: (d),(e) and the diffusive tendency of tangential momentum, and (g) local tangential wind tendency. Filled contours in (d)–(g) are shaded according to the color bar beneath the plots (m s^{-1} h^{-1}). Azimuthally averaged vertical velocity (yellow contour; 0.5 m s^{-1}), inflow and outflow (solid and dashed black contours, respectively; 1.2 m s^{-1}), the tangential wind tendency zero line (thin gray contour), and the mean location of maximum tangential wind (black star) are overlaid.

systematic relationship between the radial wind between heights of 1 and 1.5 km and the strength of the eyewall updraft. This discussion will be developed further in section 4b.

Closer inspection of the three-dimensional storm evolution also reveals times when intensity changes cannot be explained by the classical axisymmetric intensification mechanism. For example at $T + 57$, the M-surfaces are moving inward (Fig. 4b) and the mean tendency is forcing spindown of the tangential wind (Fig. 5b) within this layer of strong outflow and weak rising motion between $r = 40$ and 100 km (Figs. 5a,c,d).
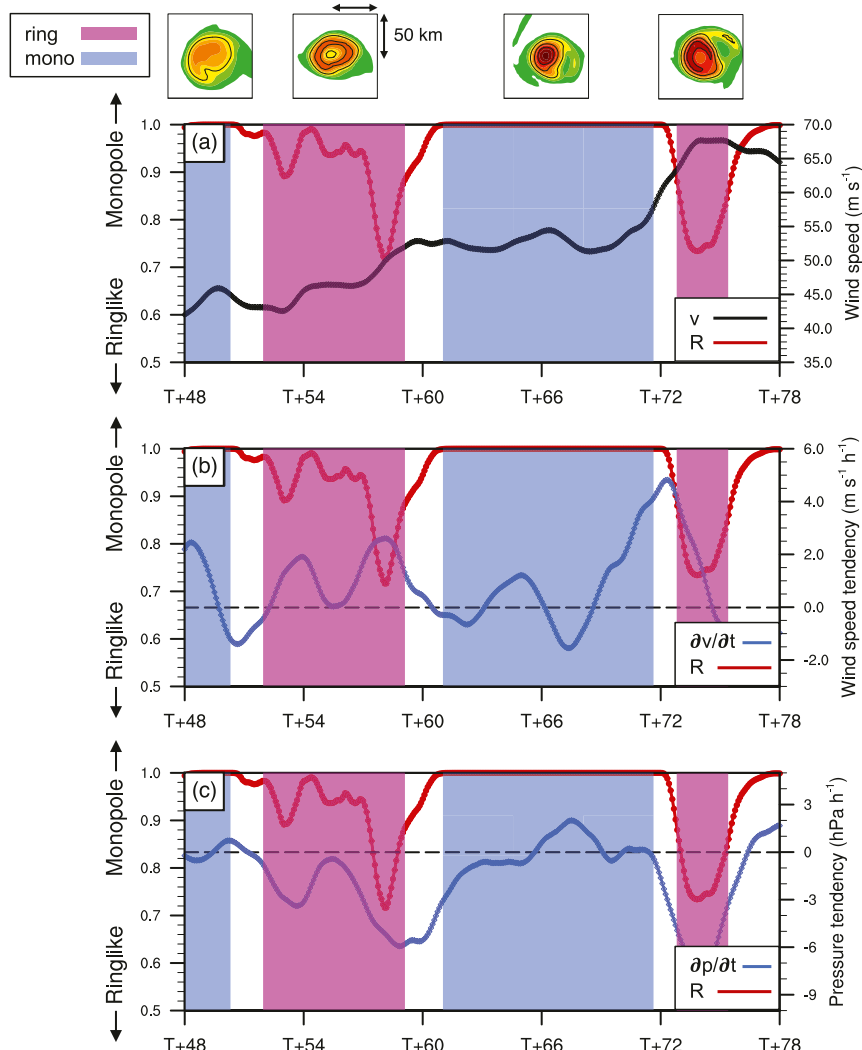
FIG. 6. Time series of the vorticity ratio R (red line; values of 1.0 represent a monopole structure, and values below 0.9 represent a ringlike structure). The panels are overlaid with the (a) maximum azimuthally averaged tangential wind (m s^{-1}), (b) tendency of the maximum azimuthally averaged tangential wind (m s^{-1} h^{-1}), and (c) mean sea level pressure tendency (hPa h^{-1}). (top) The inset panels represent the 1.5–4 km layer-averaged relative vorticity within a $1.0° \times 1.0°$ box centered on the storm center during each of the identified monopole and ringlike phases. Data are plotted for simulation em11, initialized at 1200 UTC 2 Jul 2016. The pink and blue shaded regions represent the ringlike and monopole phases, respectively.

One possibility is that the vertical advection of M is sufficient to outweigh the negative radial advection of M in this outflow layer. Alternatively, as shown in Fig. 5e, the spindown forced by the mean is opposed by the eddy tendency, resulting in weak spinup overall between $r = 50$ and 100 km (Fig. 5f).[2] This result indicates that the contribution of the eddies must not be neglected when

trying to understand the three-dimensional evolution of the storm.

Figure 6 outlines the relationship between R and the intensification rate. The inner core fluctuates between ringlike ($R <$ 1) and monopolar ($R = 1$) states, with a period of 9–12 h. Although the ringlike and monopolar states themselves last between 6 and 12 h, the transitions between these states take only between 1 and 3 h, similar to the time scales found by Kossin and Eastin (2001). During the ringlike phase when $R <$ 1, the maximum azimuthally averaged relative vorticity migrates about 10 to 15 km from the eye (Fig. 7). Conversely, the

---

[2] The degree of qualitative agreement between Figs. 5f and 5g lends authority to this interpretation.
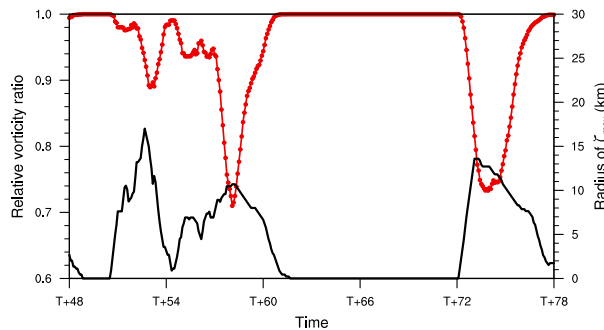
FIG. 7. Time series of the vorticity ratio R (red line; values of 1.0 represent a monopole structure, and values below 0.9 represent a ringlike structure) against the radius of the maximum azimuthally averaged 1–4 km relative vorticity (black line; km). Data are plotted for simulation em11, initialized at 1200 UTC 2 Jul 2016.

FIG. 8. Time series of the tendency of the maximum azimuthally averaged tangential wind (blue line; m s^{-1} h^{-1}). Overlaid is the radially (0–50 km) and vertically integrated contribution of the combined eddy term to the azimuthally averaged tangential wind tendency, plotted as a percentage of the contribution from the combined mean term (%). The dashed gray line represents the integral over the vertical layer between 0 and 1.5 km, and the solid gray line represents the integral over the layer between 1.5 and 8 km. Data are plotted for simulation em11, initialized at 1200 UTC 2 Jul 2016.

maximum vorticity remains at $r = 0$ km during the monopole phase when $R = 1$.

The maximum mean tangential wind (hereafter v_{max}) intensifies periodically, interspersed with periods of little change or even weakening (Figs. 6a,b). There are four pronounced periods of intensification, two of which occur in the ringlike phase ($T + 54$ and $T + 58$) and two preceding the monopole to ringlike transition ($T + 48$ and $T + 72$; Fig. 6b), with a smaller peak at $T + 65$. The ringlike to monopole transition is generally associated with near-constant or weakening v_{max} throughout (Fig. 6b). These results indicate that high-frequency (1–2 h) fluctuations in the intensification rate develop within periods characterized by ringlike and monopole structure, making it difficult to define a simple relationship between intensification rate and inner-core structure.

The minimum sea level pressure tendency exhibits a stronger relationship with R, with the most pronounced pressure falls occurring when $R < 1$ and near-constant or weak positive tendencies when $R = 1$ (Fig. 6c). The periodic changes in the inner-core relative vorticity profile are shown in the inset plots at the top of Fig. 6. These simulated ringlike to monopole transitions share qualitative similarities with the observed transitions shown in Figs. 2a and 2b, suggesting that they are representative of real-world vortex behavior.

b. Tangential momentum budget analysis of a single fluctuation

The short periods chosen to represent the ringlike and monopole phases in this section are representative of the overall behavior of the storm during each phase. Although the sign and magnitude of the tendency of v_{max} fluctuate throughout both phases (Figs. 6a,b), the respective contributions from the mean and eddy terms during the chosen periods in this section are generally representative of the contributions over all times in each phase (not shown).

In Fig. 8, the contribution of the eddy terms in Eq. (1) to the mean tangential wind tendency has been integrated radially between 0 and 50 km and vertically between the surface and 1.5 km (dashed line), and between 1.5 and 8 km (solid line). The contribution has then been expressed as a percentage of
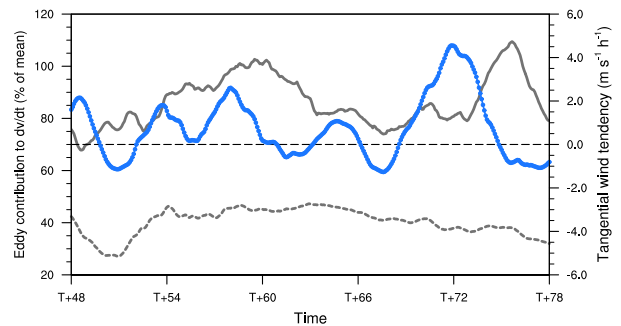
the contribution from the mean terms. Within the lowest 1.5 km, the eddies contribute between 25% and 45% of the mean total tendency, indicating that although the mean term contributes more strongly to intensity change between $T + 48$ and $T + 78$, the eddy term cannot be ignored. Between 1.5 and 8 km, the eddies contribute between 65% and 110% of the mean, showing that the contribution of the asymmetric component of the flow must be quantified to fully understand the simulated storm's intensification. Comparison with Fig. 7 suggests that for this storm at least, the contribution of the eddies is not systematically tied to changes in the inner-core structure, as was hypothesized for Katrina by Nguyen et al. (2011) and Hankinson et al. (2014). Additional analysis of the eddy terms with higher-resolution simulations may be required to determine whether these conclusions apply more generally to intensifying tropical cyclones undergoing fluctuations in inner-core structure.

1) RINGLIKE PHASE ($T + 53.5$ TO $T + 54.5$)

The key physical processes responsible for changes in the intensification rate associated with Nepartak's inner-core fluctuations are identified by analyzing the tangential momentum equation [Eq. (1)]. Similar analyses have identified the processes responsible for secondary eyewall formation in mature tropical cyclones (e.g., Abarca and Montgomery 2013; Qiu and Tan 2013; Zhu and Zhu 2014; Wang et al. 2016; Huang et al. 2018).

The eyewall updraft is located at a radius of 20–25 km from the axis of rotation (Fig. 9c), the surface-based inflow layer and the upper-level (between about 12 and 16 km) outflow layers comprise the secondary circulation (Fig. 9a), and the swirling primary circulation has a maximum between 40 and 45 m s^{-1} in the lowest 1 km (Fig. 9b), about 25 km from the storm center. Another prominent feature is the shallow outflow layer above where the surface-based inflow terminates at about 10 km radius (Fig. 9a).
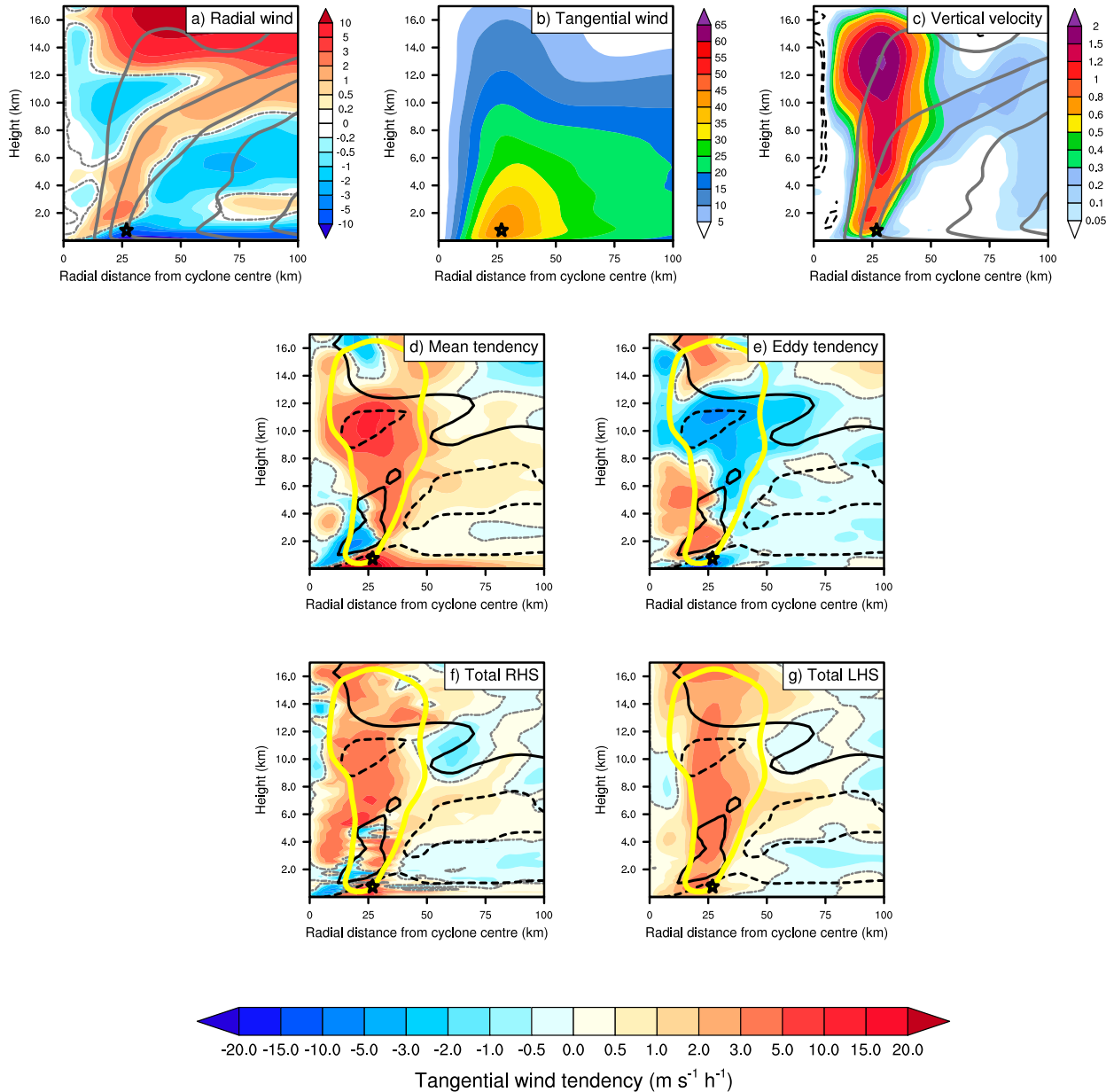
FIG. 9. Radius–height plots of the ringlike phase, calculated using data between $T + 53.5$ and $T + 54.5$ from simulation em11, initialized at 1200 UTC 2 Jul 2016, using a 5-min output interval. Azimuthally averaged (a) radial wind, (b) tangential wind, and (c) vertical velocity, all shaded according to the color bars with units m s^{-1}, with M surfaces overlaid in (a) and (c) (gray contours; 0.5 to 2.5 m^2 s^{-1}, every 0.5 m^2 s^{-1}). The radial wind zero line (thin gray contour) is overlaid on (a). Azimuthally averaged (d) combined mean radial vorticity flux and mean vertical advection of mean tangential momentum, (e) combined eddy radial vorticity flux and eddy vertical advection of eddy tangential momentum, and (f) sum of all right-hand-side terms: (d),(e) and the diffusive tendency of tangential momentum, and (g) local tangential wind tendency. Filled contours in (d)–(g) are shaded according to the color bar beneath the plots (m s^{-1} h^{-1}). Azimuthally averaged vertical velocity (yellow contour; 0.5 m s^{-1}), inflow and outflow (solid and dashed black contours, respectively; 1.2 m s^{-1}), the tangential wind tendency zero line (thin gray contour), and the mean location of maximum tangential wind (black star) are overlaid.

In general, there is good qualitative agreement between the left- and right-hand sides of the budget, away from the innermost 10–15 km between the surface and 6 km in height (Figs. 9f,g). In this region, the mean tangential wind tendency calculated using the forcing terms on the right-hand side is much larger than the local tendency. The relatively poor performance of the analyses in this region is associated with numerical errors in the computation of terms in Eq. (1). The local tangential wind tendency on the left-hand side is computed using data output every 5 min (rather than the model time step

of 75 s), and is thus an approximation. In addition, the advection and diffusive tendency terms on the right-hand side are calculated using centered spatial differences, whereas the MetUM uses a semi-Lagrangian advection scheme. These issues were noted by Persing et al. (2013, p. 12 318) and Montgomery et al. (2020) among others, indicating the existence of some intrinsic uncertainty in these types of budget calculations. Nevertheless, the general agreement between left- and right-hand sides of the budget provides strong support for our interpretation of the forcing terms on the right-hand side of Eq. (1).

The strong positive contribution of the combined mean term (Fig. 9d) to the mean tangential wind tendency in the boundary layer is dominated by the import of mean absolute vorticity by the boundary layer inflow, as in previous idealized modeling studies (e.g., Zhang et al. 2001; Bui et al. 2009; Persing et al. 2013) and simulations of real cases (e.g., Sun et al. 2013; Wang et al. 2016; Huang et al. 2018). In addition, the region of positive mean tangential wind tendency within the eyewall updraft region between 6 and 13 km (Fig. 9d) is similar to that found by Sun et al. (2013) in their study of Typhoon Sinlaku (2008), and by Persing et al. (2013) in their idealized study on the role of asymmetric processes on RI. Within the surface-based inflow layer, the mean term leads to spinup, opposed by the eddies, but between 1.5 and 8 km, the eddies are almost equal in magnitude but opposite in sign (cf. Figs. 8 and 9d,e). In particular, the eddies contribute to the spinup of the tangential wind immediately above the location of v_{max} and inside the main eyewall updraft region between 2 and 8 km (cf. Figs. 9e,f). The mean influx of relative vorticity spins up v_{max}, but the combined effect of the eddies is to deepen the cyclonic circulation and move the eyewall updraft region inward. The importance of the eddies in intensifying the swirling flow in the eyewall affirms the findings from the idealized studies of Persing et al. (2013) and Montgomery et al. (2020).

2) MONOPOLE PHASE ($T + 65$ TO $T + 66$)

In the 10.5 h between the ringlike phase and the start of the monopole phase, the eyewall has migrated inward to a position about 10–15 km from the storm center (Fig. 10c), consistent with the evolution shown in Fig. 4c. The M surfaces have moved inward (cf. Figs. 9c and 10c), coincident with an increase in v_{max} to between 50 and 55 m s^{-1} (cf. Figs. 9b and 10b). In the lowest 4 km, both the mean and eddy terms have strengthened, with tendencies now greater than 20 m s^{-1} h^{-1} (Figs. 10d,e). As a percentage of the contribution from the combined mean term to the tangential wind tendency however, the eddy contribution is similar to that in the ringlike phase (Fig. 8).

As in the ringlike phase, the combined mean term spins up the mean tangential wind at v_{max}, strongly opposed by the eddies, resulting in only weak spin up (Figs. 10d–f). Immediately above v_{max} in the eyewall updraft region between 2 and 4 km, the combined eddy term spins up the vortex (Figs. 10e,f). The role of the eddies in spinning up the mean tangential wind in this region supports the findings from the idealized studies of Persing et al. (2013) and Montgomery et al. (2020) and the case studies of real events by Smith et al. (2017)

and Leighton et al. (2018), as well as the Wang et al. (2016) study on secondary eyewall formation. Conversely, additional modeling studies on secondary eyewall formation found that the eddies played a less prominent role in spinning up the vortex above the boundary layer (e.g., Sun et al. 2013; Zhu and Zhu 2014; Huang et al. 2018). These differences could be associated with case-by-case variability, or differences in model setup between idealized studies and case studies of real events. For example, the idealized studies of Zhu and Zhu (2014) and Wang et al. (2016) lacked an environmental vorticity gradient or vertical shear.

As in the ringlike phase, the budget analyses demonstrate strong qualitative agreement, notwithstanding the relatively poor performance in the innermost 10–15 km (Figs. 10f,g). On the large scale, the qualitative similarities between the contributions from the mean and eddy terms in both ringlike and monopole phases indicate that above the surface-based inflow layer, the eddies contribute almost the same as the mean term to changes in vortex strength, during both periods of intensification and near-constant wind speed (Fig. 8). This result again shows that the contribution of the eddies to intensification must be quantified to fully understand the three-dimensional evolution of the vortex.

3) COMPARISON BETWEEN ALL PHASES

Since v_{max} is used as the metric to characterize the vortex intensity in this paper, it is appropriate to investigate processes contributing to intensity changes at the location of v_{max}. To this end, the contributions of the combined mean, eddy, and diffusion terms in Eq. (1) to the mean tangential wind tendency at the location of v_{max}, during the ringlike and monopole phases as well as the transitions between them, are shown in Table 1. Note that v_{max} is almost always located within the surface-based inflow layer where frictional forces are expected to be important. In fact, during all four phases, both the eddy and diffusion terms make a substantial contribution to the evolution of v_{max}, indicating that M is not (approximately) materially conserved at this location. For this reason, the classical mechanism of vortex spin up cannot be invoked to fully explain intensity changes. As shown earlier in Figs. 9 and 10, the eddies largely oppose the spin up of v_{max} by the mean term.

Radius–height plots of the local mean tangential wind tendency and the radial wind are shown in Figs. 11 and 12, respectively, for the four inner-core regimes. During the ringlike phase, the strongest increase in the tangential wind is relatively far inside the starting location of v_{max} (Fig. 11a). The location of v_{max} moves inward during the period, but does not follow the M surface, again indicating that M is not conserved there. This result reflects the strong contribution from the eddy term to the mean tangential wind tendency at v_{max} (Table 1), further demonstrating that we cannot use the movement of the M surfaces to predict how v_{max} will change.

The fact that v_{max} is located within the strong surface-based inflow layer in all regimes (Fig. 12) suggests that changes in v_{max} will be strongly influenced by changes in the boundary layer inflow. Indeed, inflow in this layer strengthens and deepens between the ringlike phase and the ringlike to monopole
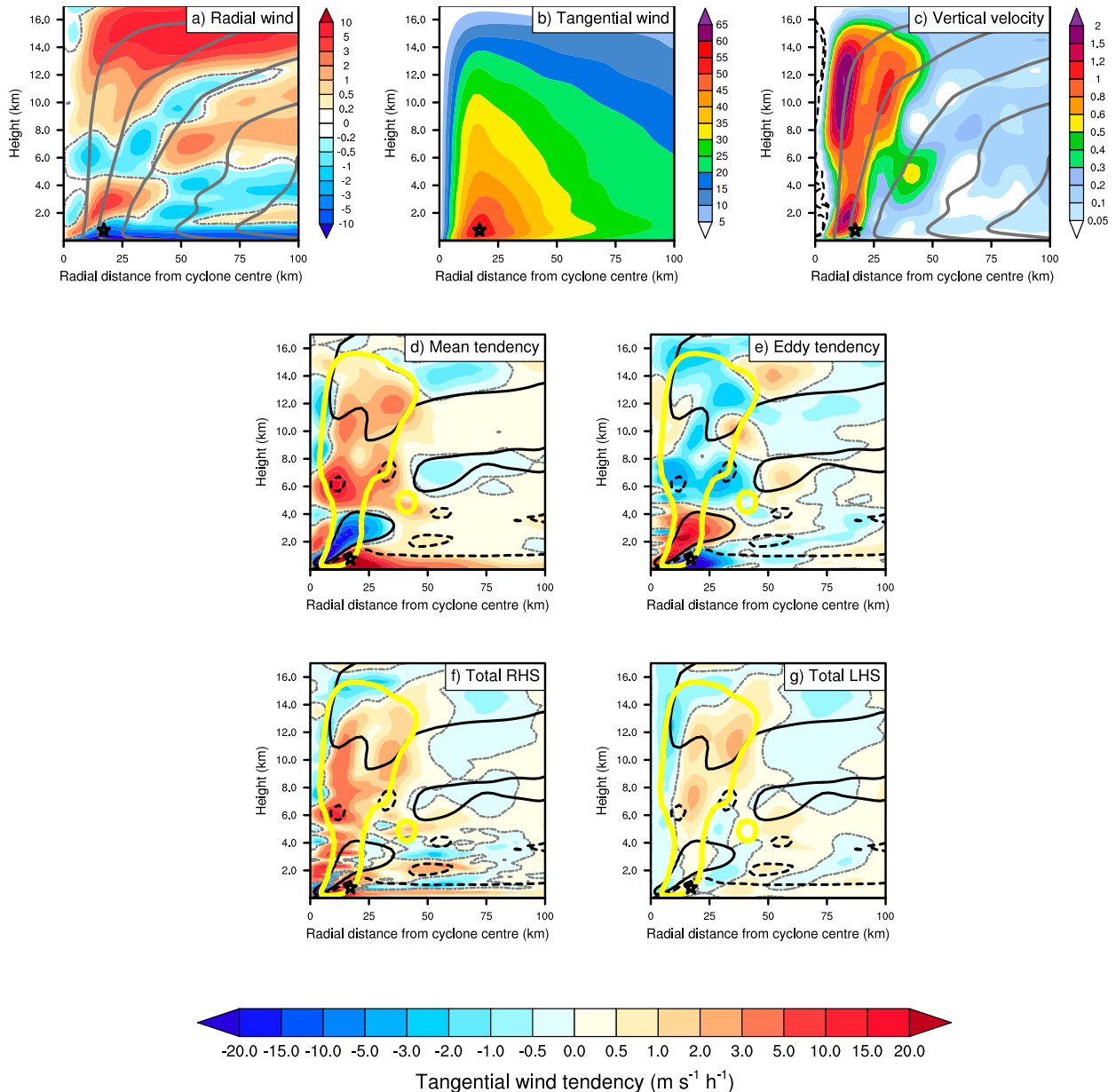
FIG. 10. As in Fig. 9, but between $T + 65$ and $T + 66$, representative of the monopole phase.

transition (cf. Figs. 12a,b), indicative of the boundary layer spinup mechanism[3] in operation. However, because the flow in this region is tightly coupled to the flow immediately above the

boundary layer and is fully nonlinear, it is difficult to separate the inflow induced by the eyewall convection from that induced by the boundary layer spinup mechanism (see discussion in Smith and Montgomery 2015, their p. 3028). During the ringlike to monopole transition, v_{max} moves little despite the tangential wind tendency at small radii strengthening relative to the ringlike phase (Fig. 11b). The inner-core region is spinning up, but v_{max} itself lies within a region where the tendency is almost zero. This pattern is consistent with a mixing of the highest momentum air from the eyewall into the eye (e.g., Schubert et al. 1999).

The tangential wind tendencies are much weaker during the monopole phase (Fig. 11c). As in the ringlike phase, v_{max}

---

[3] In the boundary layer spinup mechanism, air parcels in the boundary layer lose M to the surface as they spiral inward and their radius decreases. However, if the air parcels spiral inward quickly enough, the decrease in radius will be larger than the decrease in M and the tangential wind $[v = (M/r) - (1/2)fr^2]$ can actually increase, exceeding its value immediately above the boundary layer (see discussion and associated references in Montgomery and Smith (2017), their p. 549).

TABLE 1. Contributions of the combined mean and eddy and diffusion terms in Eq. (1) to the mean tangential wind tendency at the location of maximum wind (percentage of total tendency), and the amount of time that the maximum wind was located within the lower-tropospheric inflow layer (percentage of time within each period). Contributions are calculated during the ringlike phase ($T + 52$ to $T + 55$), the ringlike to monopole transition ($T + 58.5$ to $T + 60.5$), the monopole phase ($T + 62$ to $T + 67$), and the monopole to ringlike transition ($T + 71$ to $T + 73$). The calculations use simulation em11, initialized at 1200 UTC 2 Jul 2016, with a 5-min output interval.

Inner-core structure	Mean term (% of total)	Eddy term (% of total)	Diffusion term (% of total)	v_{max} within the inflow (%)
Ringlike	50.0	35.3	14.7	91.8
Ring to mono transition	60.5	32.6	6.9	100.0
Monopole	61.0	32.1	6.9	98.3
Mono to ring transition	58.0	28.4	13.6	100.0

moves relative to the M surface at its starting point, indicative of the nonconservation of M related to the strong contribution of the asymmetric component of the flow (Table 1). Although the inflow layer remains strong, the sloping region of outflow immediately above it strengthens too, indicating that the updraft is not able to evacuate all the mass converging in the boundary layer (Fig. 12c). During the monopole to ringlike transition, there is strong spindown near the rotation axis and strong spinup at v_{max} (Fig. 11d). The inward radial movement of the M surface shows that the vortex is spinning up through the depth of the lowest 5 km, not just at v_{max} (Fig. 11d). However, the extension of the region of enhanced outflow outside the main eyewall updraft region indicates that, as in the monopole phase, the updraft is not able to evacuate all the mass converging in the boundary layer (Fig. 12d), providing a possible brake on the intensification rate of the storm (see e.g., Kilroy et al. 2016, p. 496).

The ability of the eyewall updraft to evacuate the mass converging in the boundary layer is quantified by calculating the difference in azimuthally averaged, radially integrated (between 0 and 50 km) vertical mass flux over two layers, at 1.5 and 6 km, respectively (Fig. 13). Positive values indicate that the eyewall updraft is evacuating mass at a rate exceeding that at which mass is converging in the boundary layer, and vice versa. A 2-h running average has been applied to each of these datasets to smooth out any high-frequency fluctuations, similar to Kilroy et al. (2016). The mass flux difference has two pronounced peaks near $T + 52$ and $T + 59$ during the ringlike phase, and a third peak near $T + 70$. These peaks are well correlated with periods of spinup of the maximum tangential wind (Fig. 13). This correlation suggests that during periods of pronounced spinup, the eyewall updraft is more than able to evacuate the mass converging in the boundary layer and, as a result, draws air inward above the boundary layer, enabling the classical spinup mechanism to operate there. Furthermore, as shown earlier in Fig. 4c, there are short periods in the storm's life cycle when the eyewall updraft weakens, such as near $T + 49$, $T + 54$ and $T + 67$. These periods are accompanied by peaks in the outflow extending outward from the eyewall updraft region (Fig. 4b) and dips in the vertical mass flux (Fig. 13), indicating that the convection at these times is unable to evacuate the mass converging in the boundary layer. These intervals are associated with a reduction in the storm's intensification rate, further suggesting a relationship between the strength of the eyewall updraft and the intensification rate (Fig. 13).

However, the relationship between the inner-core structure and the mass flux is more complicated than that suggested by this simple hypothesis. Increases in the intensification rate at v_{max}, such as that seen in the monopole to ringlike transition between $T + 71$ and $T + 73$ (Fig. 12d), can result also in enhanced outflow immediately above the inflow layer, resulting in the eyewall updraft evacuating a lower percentage of the converging mass in the boundary layer. In addition, inflow is not confined to the boundary layer, with the classical spinup mechanism in evidence above the boundary layer also during the ringlike to monopole transition (Fig. 12b) and in the monopole phase (Fig. 12c).

c. Composite analysis of intensity change

As discussed at the beginning of section 4, composite diagnostics are calculated using 1-h data from 18 inner-core fluctuations across 16 forecasts. All time intervals in this composite dataset are split into four regimes based on the time tendency of R (Fig. 14a).[4] The tendency of v_{max} is largest and positive in the monopole to ringlike transition and in the ringlike phase (Fig. 14c). The mean rate of intensification is smaller during the ringlike to monopole transition and the monopole phase. The signal for a more pronounced increase in v_{max} during the ringlike phase, and a tendency closer to zero during the monopole phase, is consistent with previous observational (e.g., Reasor et al. 2000, 2009; Kossin and Eastin 2001) and modeling (e.g., Nguyen et al. 2011; Hankinson et al. 2014) studies as well as the composite study by Rogers et al. (2013).

However, these results do not provide unequivocal support for this relationship between inner-core structure and intensification rate. Both positive and negative v_{max} tendencies occur in all four regimes (Fig. 14c). The inference from Figs. 14b and 14c is that despite the existence of a signal in both the key metrics for intensification—the v_{max} and minimum sea level pressure tendencies—the intensification rate will not show the same relationship with inner-core structure in all ringlike or monopole phases. The overlapping distributions and the large

---

[4] Because $\partial R/\partial t$ at each time interval is calculated using centered finite differences and some regimes contain only a single time interval, there are instances when the values in the ringlike and monopole phases fluctuate either side of zero, which accounts for the spread of values in the ringlike and monopole phase box-and-whisker plots in (Fig. 14a).
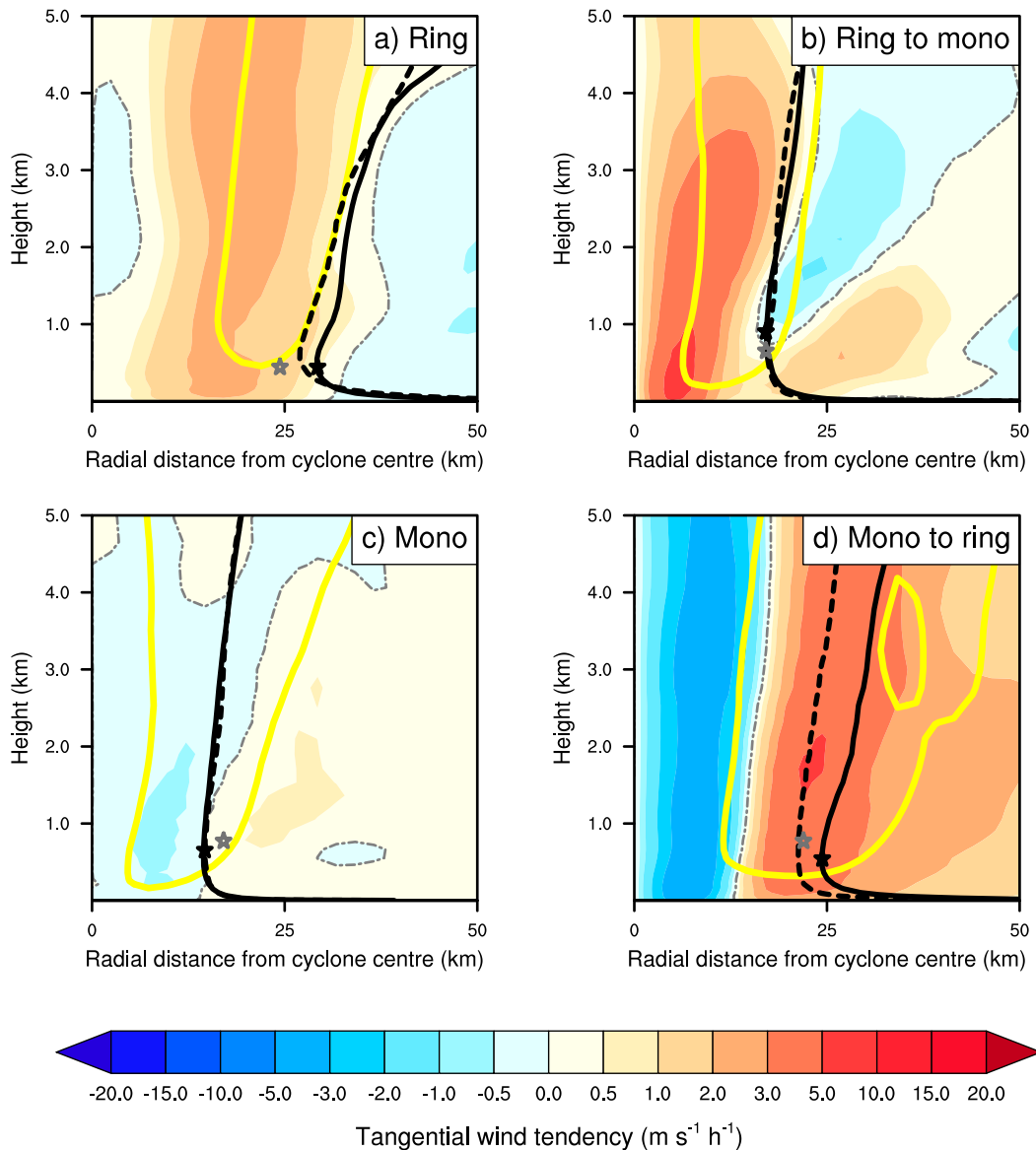
FIG. 11. Azimuthally averaged tangential wind tendency (filled contours, $m\,s^{-1}\,h^{-1}$) from simulation em11, initialized at 1200 UTC 2 Jul 2016, using a 5-min output interval, for (a) the ringlike phase ($T + 52$ to $T + 55$), (b) the ringlike to monopole transition ($T + 58.5$ to $T + 60.5$), (c) the monopole phase ($T + 62$ to $T + 67$), and (d) the monopole to ringlike transition ($T + 71$ to $T + 73$). As in Fig. 9, azimuthally averaged vertical velocity (yellow contour; $0.5\,m\,s^{-1}$) and the tangential wind tendency zero line (thin gray contour) are overlaid. The starting and ending positions of the location of maximum tangential wind are overlaid with a black and a gray star, respectively. The azimuthally averaged M surface at the starting position of the location of maximum wind is overlaid with a solid black contour ($m^2\,s^{-1}$). The dashed black contour represents the position of this same M surface at the end of the period.

range, particularly in the minimum sea level pressure tendency in the monopole phase (Fig. 14c), further suggest that strong variability also exists within each regime, perhaps on finer spatial and temporal scales than those resolved in these simulations.

The minimum sea level pressure tendency is most strongly negative in the ringlike phase and the ringlike to monopole transition (Fig. 14b), suggesting that spinup of v_{max} will not always occur in tandem with pressure falls. During the monopole

phase, the pressure tendency is weak and positive (Fig. 14b), with a large range. Kossin and Schubert (2001) used barotropic simulations to show that as idealized ringlike vortices become increasingly monopolar, vorticity mixing between the eye and eyewall can lead to strong surface pressure falls. The overall weak positive pressure tendency during the monopole phase in our simulations (Fig. 14b) suggests that processes other than vorticity mixing are occurring and opposing the theorized negative tendency due to mixing. However, more detailed
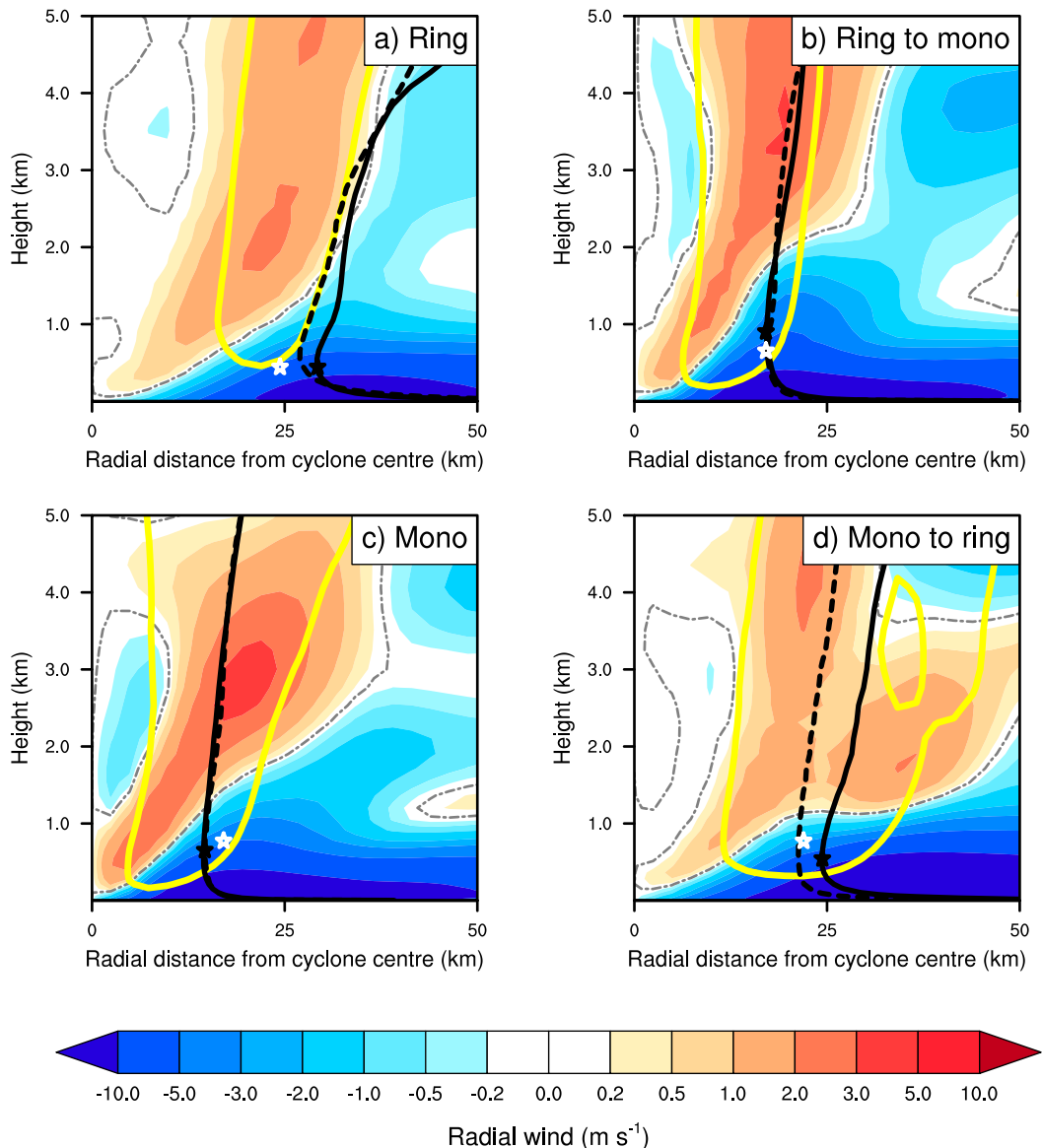
FIG. 12. Azimuthally averaged radial wind (filled contours, m s^{-1}) from simulation em11, initialized at 1200 UTC 2 Jul 2016, using a 5-min output interval, for (a) the ringlike phase ($T + 52$ to $T + 55$), (b) the ringlike to monopole transition ($T + 58.5$ to $T + 60.5$), (c) the monopole phase ($T + 62$ to $T + 67$), and (d) the monopole to ringlike transition ($T + 71$ to $T + 73$). Azimuthally averaged vertical velocity (yellow contour; 0.5 m s^{-1}) and the radial wind zero line (thin gray contour) are overlaid. The starting and ending positions of the location of maximum tangential wind are overlaid with a black and a white star, respectively. The azimuthally averaged M surface at the starting position of the location of maximum wind is overlaid with a solid black contour (m^2 s^{-1}). The dashed black contour represents the position of this same M surface at the end of the period.

analysis of the relationship between R and the pressure tendency is outside the scope of this paper.

d. Composite tangential momentum budget analysis

In both the ringlike and monopole phases, the contributions from the mean and eddy terms are qualitatively similar to those in the analysis of the single simulation (cf. Figs. 9, 10, and 15). The mean term spins up the tangential wind at the location of $v_{\max}$, opposed by the eddies, whereas the eddy term contributes

to the deepening of the cyclonic circulation between 1.5 and 6 km. The contribution of the eddies as a percentage of the mean is qualitatively similar in both phases as in the analysis of a single simulation (Fig. 8), both within the lowest 1.5 km (35% in both the monopole and ringlike phases) and between 1.5 and 8 km (84% in the ringlike phase, 90% in the monopole phase). These results demonstrate the strong influence of the asymmetric component of the flow on the mean tangential wind tendency during intensification, irrespective of inner-core structure.
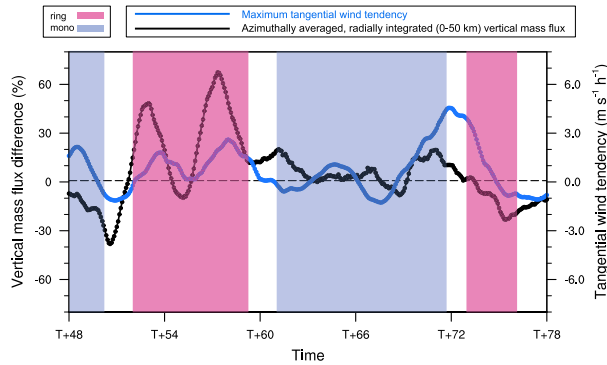
FIG. 13. Time series of the difference in the azimuthally averaged, radially integrated (between 0 and 50 km) vertical mass flux between two layers, the first centered on 6 km and the second centered on 1.5 km (black contour), plotted as a percentage of the vertical mass flux over the lower, 1.5 km, layer (%). The plot is overlaid with the tendency of the maximum azimuthally averaged tangential wind (blue contour; $m\,s^{-1}\,h^{-1}$). Data are plotted for simulation em11, initialized at 1200 UTC 2 Jul 2016, using a 5-min output interval. A 2-h running average is applied to both the mass flux and the tangential wind tendency. The pink and blue shaded regions represent the ringlike and monopole phases, respectively.

Composite plots of the local tangential wind tendency for all regimes (Fig. 16) also reveal qualitatively similar patterns to those found for the single simulation (Fig. 11), albeit with generally weaker tendencies. This qualitative agreement suggests that although strong variability exists within each regime (Fig. 14), the oscillations in the mean tangential wind tendency are intrinsically linked with the observed inner-core structural changes, as hypothesized by Kossin and Eastin (2001).

Typical changes in the intensification rate accompanying fluctuations in the inner-core structure are shown in Fig. 17, which is a schematic Hovmöller plot based on the data from all the ensemble forecasts of Nepartak. The storm's inner core

fluctuates between ringlike and monopole states, characterized by azimuthally averaged relative vorticity with a maximum some distance from the eye and in the eye, respectively (Fig. 17c). During the ringlike phase, the tangential wind first spins up at the location of v_{max}, accompanied by strong pressure falls (Figs. 17a,b). Spinup continues inside the location of v_{max} during the ringlike to monopole transition but weakens at v_{max}, as the eyewall updraft moves inward (Fig. 17a). During the monopole phase the pressure and tangential wind tendencies fall to near zero, first at v_{max} and then at progressively smaller radii. As the inner-core vorticity profile becomes more ringlike again, spinup first recommences outside v_{max} and then at progressively smaller radii. This evolution, which generally takes between 6 and 12 h, shares strong qualitative similarities with that described by Nguyen et al. (2011) and Hankinson et al. (2014) in their studies on vacillation cycles.

5. Discussion

Following the tangential momentum equation analysis in section 4, a desirable next step would be to determine the differences between the storms with and without inner-core fluctuations, and the characteristics of their respective environments. Such an analysis could determine the extent to which these fluctuations are influenced by changes in the environmental flow, in the process providing useful forecast guidance on their likelihood of development during different background flow regimes.

However, there is strong evidence that phenomena that are intrinsically linked to tropical cyclone intensity change on time scales of several hours or less have a strong stochastic element and are thus inherently unpredictable (e.g., Nguyen et al. 2008). Furthermore, the low-level moisture field often displays strong variability on small spatial scales (e.g., Weckwerth 2000). Both ensemble-based studies of specific storms (Sippel and Zhang 2008; Zhang and Sippel 2009;
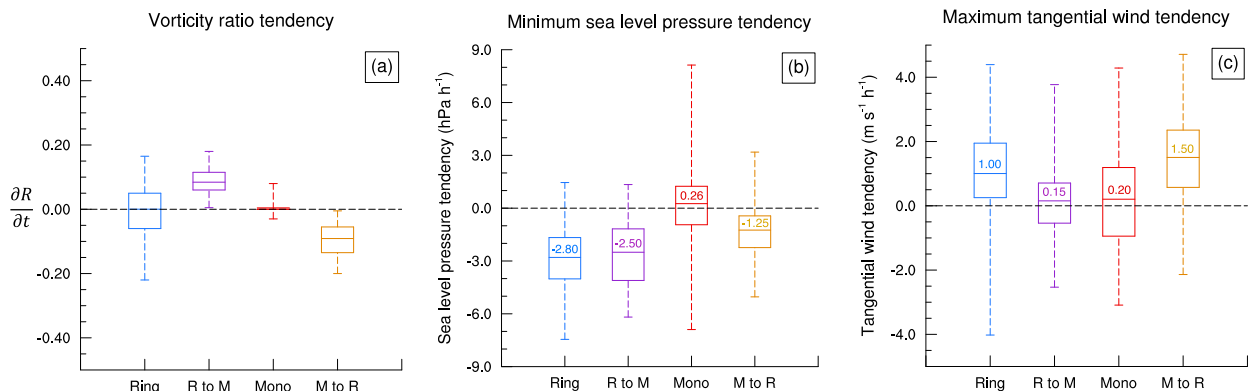

FIG. 14. Box-and-whisker plots for the ringlike phase (Ring), the ringlike to monopole transition (R to M), the monopole phase (Mono), and the monopole to ringlike transition (M to R). (a) Time tendency of the vorticity ratio (R). For a ringlike inner core with maximum relative vorticity some distance from the center, R is minimized, and for a monopolar inner core with maximum relative vorticity at its center, R is maximized. The time tendency in both these phases will therefore be close to zero. The ringlike to monopole and monopole to ringlike transitions are defined by positive and negative time tendencies of R, respectively. (b) Minimum sea level pressure tendency ($hPa\,h^{-1}$). (c) Tangential wind tendency ($m\,s^{-1}\,h^{-1}$). The tangential wind tendency is calculated using the maximum tangential wind at each time on any model height level. All plots are produced using data from 18 inner-core fluctuations over 16 simulations.
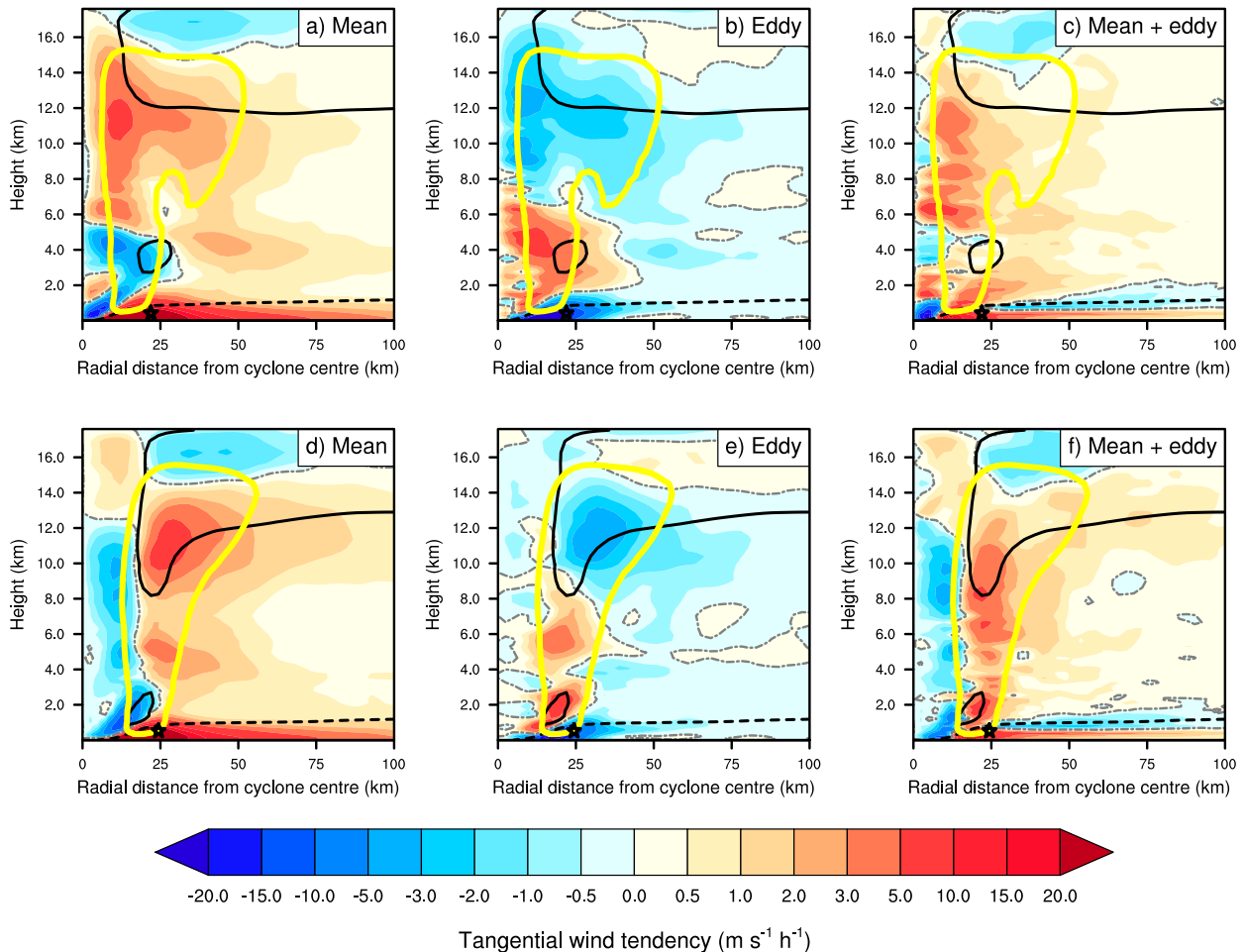
FIG. 15. Azimuthally averaged (a) combined mean radial vorticity flux and mean vertical advection of mean tangential momentum, (b) combined eddy radial vorticity flux and eddy vertical advection of eddy tangential momentum, and (c) sum of (a) and (b), for the monopole phase, calculated using data from the same 18 inner-core fluctuations over 16 simulations as in Fig. 14. (d)–(f) As in (a)–(c), but for the ringlike phase. The momentum budget terms are shaded according to the color bar (m s^{-1} h^{-1}). Azimuthally averaged vertical velocity (yellow contour; 0.5 m s^{-1}), inflow and outflow (solid and dashed black contours, respectively; ±1.2 m s^{-1}), the tangential wind tendency zero line (thin gray contour), and the mean location of maximum tangential wind (black star) are overlaid in (a)–(c) for the monopole phase and in (d)–(f) for the ringlike phase.

Sippel and Zhang 2010), and idealized studies (e.g., Nguyen et al. 2008; Tao and Zhang 2015) have argued that stochastic variability associated with moist convection, often smaller than the magnitude of typical observation- and analysis-based error, generates rapid upscale error growth that intrinsically limits tropical cyclone predictability. For example, in a 60-member ensemble forecast of Hurricane Edouard (2017), Munsell et al. (2017) found that imperceptible differences in initial condition moisture and winds resulted in a 60-h spread in the timing of RI onset between ensemble members. In a similar vein, Judt et al. (2016) and Ying and Zhang (2017) demonstrated that convective processes on the scale of the tropical cyclone inner core have predictability limits of under 12 h. In their modeling studies of Hurricane Katrina (2005), Nguyen et al. (2011) and Hankinson et al. (2014) hypothesized that vacillation cycles are influenced by stochastic variability. They suggested that the breakdown of the ringlike inner-core structure into a monopole is driven by

a combination of barotropic and convective instabilities, which work in tandem to amplify small convective perturbations on time scales of around 6 h.

The foregoing evidence suggests that the realistic initial condition perturbations to the boundary layer moisture, temperature and wind fields present in these simulations could lead to vastly different convective configurations even 12 h after initialization, and that these differences could influence the likelihood of inner-core fluctuations. The time scales (6–12 h) on which these fluctuations occur and the strong contribution of eddy processes to the mean tangential wind tendency, irrespective of inner-core structure (Fig. 8), suggests that they are more strongly driven by stochastic variability than by the environmental background state. In developing a method to understand why fluctuations develop in some forecasts and not others, there must be two areas of focus. First, it is important to identify the differences in environmental characteristics such
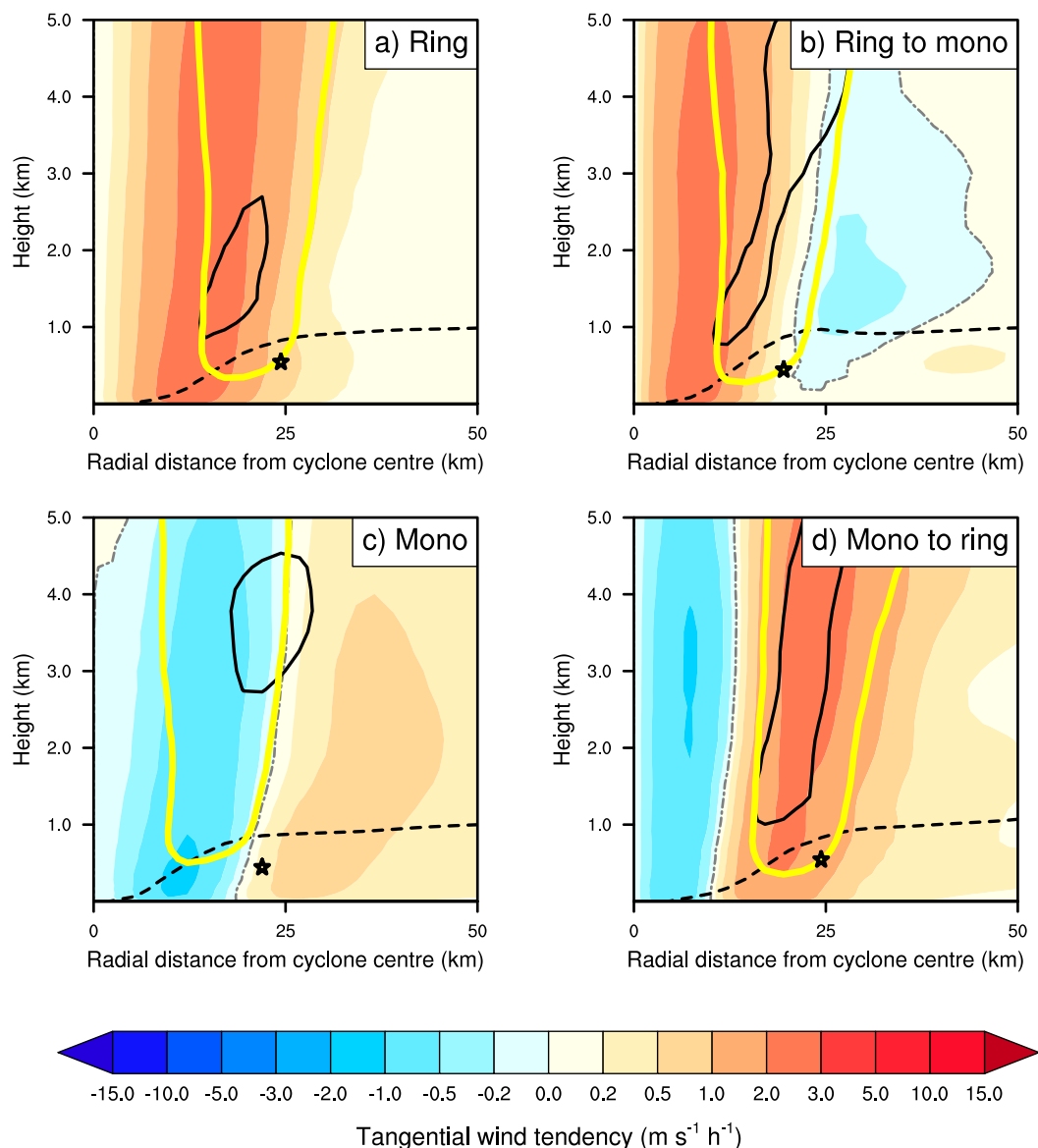
FIG. 16. Azimuthally averaged tangential wind tendency for (a) the ringlike phase, (b) the ringlike to monopole transition, (c) the monopole phase, and (d) the monopole to ringlike transition. The plots are produced using data from 18 simulated inner-core fluctuations over 16 simulations, as in Figs. 14 and 15. As in Fig. 9, azimuthally averaged vertical velocity (yellow contour; 0.5 m s^{-1}), inflow and outflow (solid and dashed black contours, respectively; 1.2 m s^{-1}), the tangential wind tendency zero line (thin gray contour), and the mean position of the location of maximum tangential wind (black star) are overlaid.

as lower-tropospheric equivalent potential temperature or SST, on the scale of the storm and larger, for a large number of storms that produce fluctuations versus those that do not. Given that the intrinsic predictability of tropical cyclones is hypothesized to vary with quantities that include vertical wind shear (e.g., Zhang and Tao 2013) and SST (e.g., Tao and Zhang 2014), the selection of these cases should be guided by such large-scale environmental characteristics. Second, the generation of convective-scale ensemble spread by perturbing the model physics (e.g., Torn 2016), rather than relying solely on initial condition uncertainty, would allow for a more thorough

investigation of the importance of stochastic variability of moist convection on the development of inner-core fluctuations.

6. Conclusions

This study investigated the key physical processes responsible for inner-core structural changes and associated fluctuations in the intensification rate for a recent, high-impact western North Pacific tropical cyclone that rapidly intensified [Nepartak (2016)], using four, 12-member convection-permitting MetUM ensemble simulations. Fluctuations between ringlike and

a) Tangential wind tendency

b) Sea level pressure tendency
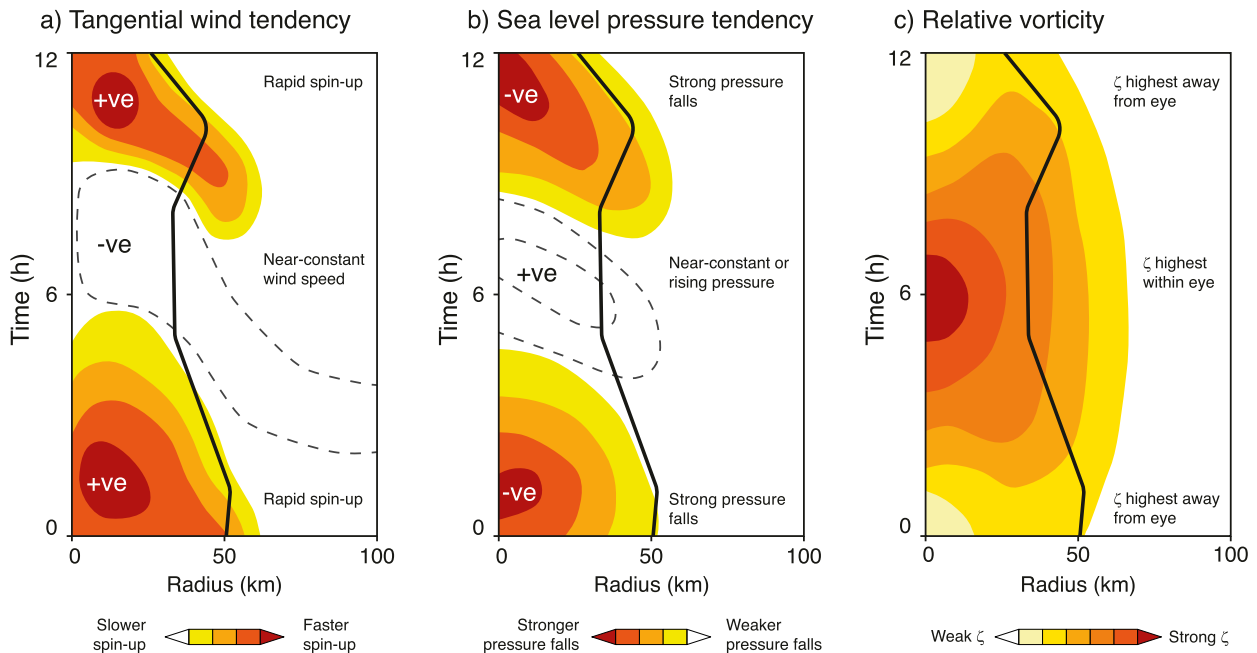
c) Relative vorticity

FIG. 17. Schematic Hovmöller plot of the typical azimuthally averaged (a) lower-tropospheric tangential wind tendency, (b) minimum sea level pressure tendency, and (c) lower-tropospheric relative vorticity associated with the fluctuations in the inner-core structure analyzed herein. Quantities are shaded according to the color bars, and the radius of maximum tangential wind is overlaid (black contour).

monopole inner-core states with a period of about 16 h occurred in 60% of ensemble simulations.

Tangential momentum equation analysis of a single fluctuation using data output at 5-min intervals revealed that during the ringlike phase, the local tendency of mean tangential wind near the location of maximum wind was generally positive. During the monopole phase the tendency was closer to zero. In both phases, the combined mean term spun up the vortex at the location of maximum wind, whereas the combined eddy term spun up the vortex above the location of maximum wind, deepening the storm's cyclonic circulation. In both phases, the integrated contribution from the combined eddy term to the mean tangential wind tendency was over 80% of that from the combined mean term, above the surface-based inflow layer. The consistently strong contribution from the combined eddy term shows that to ignore the eddies would lead to an incomplete understanding of the three-dimensional evolution of the storm. Calculations of the azimuthally averaged, radially integrated vertical mass flux at 1.5 and 6 km suggest that periods of less pronounced intensification are accompanied by a weaker eyewall updraft, outflow above the boundary layer and a reduced ability of this updraft to evacuate the mass converging in the boundary layer.

Composite analyses calculated using data from 18 fluctuations over 16 simulations revealed a tendency for the maximum tangential wind to increase most rapidly during the monopole to ringlike transition and in the ringlike phase, with the tendency closer to zero during the monopole phase. The minimum sea level pressure tendency was most negative during the ringlike phase and the ringlike to monopole transition. These results are largely in agreement with previous observational

and modeling studies. There was a large spread in both tangential wind and sea level pressure tendencies in all phases however, suggestive of strong variability both between fluctuations and within individual phases, perhaps on finer spatial and temporal (<1 h) scales than those resolved by the 4.4 km ensemble simulations.

The next logical steps are twofold. The first step would be to generalize these results by identifying fluctuations between ringlike and monopole states in a large number of tropical cyclones undergoing RI, using convection-permitting ensemble simulations. In this study, fluctuations developed in each of the four 12-member ensemble simulations, indicating that the model is able to adequately capture the changes in inner-core structure and intensification rate. Given this fact, an important future step in the development of this research area, which would also link the forecast and research communities, could involve the identification of these fluctuations in real-time ensemble forecasts using the simple methods described herein. The successful implementation of this method would require data to be output every 1 h, so would be storage-intensive, but would quickly build up a database of simulated cases from which robust, statistical relationships with sea level pressure and maximum tangential wind tendencies could be calculated. This step would also begin to contextualize the results herein with those from the studies on vacillation cycles by Nguyen et al. (2011) and Hankinson et al. (2014). The second step would be to run a convection-permitting ensemble simulation for an existing case for which ringlike to monopole fluctuations have been observed, at even higher spatial resolution (<1 km grid spacing) and using an output interval < 5 min, to quantify the contribution of the eddies in even greater detail. Together,

these types of approaches can enhance our understanding of the key physical processes driving inner-core fluctuations and provide systematic guidance to forecasters concerned about the impacts of tropical cyclones undergoing RI.

Data availability statement. The Met Office Unified Model used in these simulations is not publicly accessible. The International Best Track Archive for Climate Stewardship dataset used to produce Fig. 1 can be accessed online at https://www.ncdc.noaa.gov/ibtracs/. The Morphed Integrated Microwave Imagery at the Cooperative Institute for Meteorological Satellite Studies satellite product used to produce Fig. 2 are available online at http://tropic.ssec.wisc.edu/real-time/mimic-tc/2016_02W/.

REFERENCES

Abarca, S. F., and M. T. Montgomery, 2013: Essential dynamics of secondary eyewall formation. *J. Atmos. Sci.*, **70**, 3216–3230, https://doi.org/10.1175/JAS-D-12-0318.1.

Arakawa, A., and V. R. Lamb, 1977: Computational design of the basic dynamical processes of the UCLA general circulation. *Methods Comput. Phys.*, **17**, 173–265, https://doi.org/10.1016/B978-0-12-460817-7.50009-4.

Bishop, C. H., B. J. Etherton, and S. J. Majumdar, 2001: Adaptive sampling with the ensemble transform Kalman filter. Part I: Theoretical aspects. *Mon. Wea. Rev.*, **129**, 420–435, https://doi.org/10.1175/1520-0493(2001)129<0420:ASWTET>2.0.CO;2.

Black, P. G., and Coauthors, 2007: Air–sea exchange in hurricanes: Synthesis of observations from the Coupled Boundary Layer Air–Sea Transfer Experiment. *Bull. Amer. Meteor. Soc.*, **88**, 357–374, https://doi.org/10.1175/BAMS-88-3-357.

Bowler, N. E., A. Arribas, K. R. Mylne, K. B. Robertson, and S. E. Beare, 2008: The MOGREPS short-range ensemble prediction system. *Quart. J. Roy. Meteor. Soc.*, **134**, 703–722, https://doi.org/10.1002/qj.234.

——, ——, S. E. Beare, K. R. Mylne, and G. J. Shutts, 2009: The local ETKF and SKEB: Upgrades to the MOGREPS short-range ensemble prediction system. *Quart. J. Roy. Meteor. Soc.*, **135**, 767–776, https://doi.org/10.1002/qj.394.

Bui, H. H., R. K. Smith, M. T. Montgomery, and J. Peng, 2009: Balanced and unbalanced aspects of tropical cyclone intensification. *Quart. J. Roy. Meteor. Soc.*, **135**, 1715–1731, https://doi.org/10.1002/qj.502.

Bush, M., and Coauthors, 2020: The first Met Office Unified Model/JULES regional atmosphere and land configuration, RAL1. *Geosci. Model Dev.*, **13**, 1999–2029, https://doi.org/10.5194/gmd-13-1999-2020.

Charney, J. G., and N. A. Phillips, 1953: Numerical integration of the quasi-geostrophic equations for barotropic and simple baroclinic flows. *J. Meteor.*, **10**, 71–99, https://doi.org/10.1175/1520-0469(1953)010<0071:NIOTQG>2.0.CO;2.

Corbosiero, K. L., J. Molinari, and M. L. Black, 2005: The structure and evolution of Hurricane Elena (1985). Part I: Symmetric intensification. *Mon. Wea. Rev.*, **133**, 2905–2921, https://doi.org/10.1175/MWR3010.1.

——, ——, and A. R. Aiyyer, 2006: The structure and evolution of Hurricane Elena (1985). Part II: Convective asymmetries and evidence for vortex Rossby waves. *Mon. Wea. Rev.*, **134**, 3073–3091, https://doi.org/10.1175/MWR3250.1.

Cram, T. A., J. Persing, M. T. Montgomery, and S. A. Braun, 2007: A Lagrangian trajectory view on transport and mixing processes between the eye, eyewall, and environment using a high-resolution simulation of Hurricane Bonnie (1998). *J. Atmos. Sci.*, **64**, 1835–1856, https://doi.org/10.1175/JAS3921.1.

Cullen, M. J. P., 1993: The unified forecast/climate model. *Meteor. Mag.*, **122**, 81–94.

DeMaria, M., C. R. Sampson, J. A. Knaff, and K. D. Musgrave, 2014: Is tropical cyclone intensity guidance improving? *Bull. Amer. Meteor. Soc.*, **95**, 387–398, https://doi.org/10.1175/BAMS-D-12-00240.1.

Guinn, T. A., and W. H. Schubert, 1993: Hurricane spiral bands. *J. Atmos. Sci.*, **50**, 3380–3403, https://doi.org/10.1175/1520-0469(1993)050<3380:HSB>2.0.CO;2.

Hankinson, M. C. N., M. J. Reeder, N. E. Davidson, and K. Puri, 2014: Vacillation cycles in simulations of Hurricane Katrina. *Quart. J. Roy. Meteor. Soc.*, **140**, 1878–1888, https://doi.org/10.1002/qj.2275.

Heming, J., 2016: Met Office Unified Model tropical cyclone performance following major changes to the initialization scheme and a model upgrade. *Wea. Forecasting*, **31**, 1433–1449, https://doi.org/10.1175/WAF-D-16-0040.1.

Hendricks, E. A., and W. H. Schubert, 2010: Adiabatic rearrangement of hollow PV towers. *J. Adv. Model. Earth Syst.*, **2**, 1–19, https://doi.org/10.3894/JAMES.2010.2.8.

——, B. D. McNoldy, and W. H. Schubert, 2012: Observed inner-core structural variability in Hurricane Dolly (2008). *Mon. Wea. Rev.*, **140**, 4066–4077, https://doi.org/10.1175/MWR-D-12-00018.1.

——, W. H. Schubert, Y.-H. Chen, H.-C. Kuo, and M. S. Peng, 2014: Hurricane eyewall evolution in a forced shallow-water model. *J. Atmos. Sci.*, **71**, 1623–1643, https://doi.org/10.1175/JAS-D-13-0303.1.

Huang, Y.-H., C.-C. Wu, and M. T. Montgomery, 2018: Concentric eyewall formation in Typhoon Sinlaku (2008). Part III: Momentum budget analyses. *J. Atmos. Sci.*, **75**, 3541–3563, https://doi.org/10.1175/JAS-D-18-0037.1.

Jin, H., M. S. Peng, Y. Jin, and J. D. Doyle, 2014: An evaluation of the impact of horizontal resolution on tropical cyclone predictions using COAMPS-TC. *Wea. Forecasting*, **29**, 252–270, https://doi.org/10.1175/WAF-D-13-00054.1.

Judt, F., S. S. Chen, and J. Berner, 2016: Predictability of tropical cyclone intensity: Scale-dependent forecast error growth in high-resolution stochastic kinetic-energy backscatter ensembles. *Quart. J. Roy. Meteor. Soc.*, **142**, 43–57, https://doi.org/10.1002/qj.2626.

Kaplan, J., and M. DeMaria, 2003: Large-scale characteristics of rapidly intensifying tropical cyclones in the North Atlantic basin. *Wea. Forecasting*, **18**, 1093–1108, https://doi.org/10.1175/1520-0434(2003)018<1093:LCORIT>2.0.CO;2.

——, ——, and J. A. Knaff, 2010: A revised tropical cyclone rapid intensification index for the Atlantic and eastern North Pacific

basins. *Wea. Forecasting*, **25**, 220–241, https://doi.org/10.1175/2009WAF2222280.1.

Kilroy, G., R. K. Smith, and M. T. Montgomery, 2016: Why do model tropical cyclones grow progressively in size and decay in intensity after reaching maturity? *J. Atmos. Sci.*, **73**, 487–503, https://doi.org/10.1175/JAS-D-15-0157.1.

Knapp, K. R., M. C. Kruk, D. H. Levinson, H. J. Diamond, and C. J. Neumann, 2010: The International Best Track Archive for Climate Stewardship (IBTrACS): Unifying tropical cyclone data. *Bull. Amer. Meteor. Soc.*, **91**, 363–376, https://doi.org/10.1175/2009BAMS2755.1.

Kossin, J. P., and M. D. Eastin, 2001: Two distinct regimes in the kinematic and thermodynamic structure of the hurricane eye and eyewall. *J. Atmos. Sci.*, **58**, 1079–1090, https://doi.org/10.1175/1520-0469(2001)058<1079:TDRITK>2.0.CO;2.

——, and W. H. Schubert, 2001: Mesovortices, polygonal flow patterns, and rapid pressure falls in hurricane-like vortices. *J. Atmos. Sci.*, **58**, 2196–2209, https://doi.org/10.1175/1520-0469(2001)058<2196:MPFPAR>2.0.CO;2.

Kundu, P. K., and I. M. Cohen, 2002: *Fluid Mechanics*. 2nd ed. Elsevier, 730 pp.

Lee, C.-Y., M. K. Tippett, A. H. Sobel, and S. J. Camargo, 2016: Rapid intensification and the bimodal distribution of tropical cyclone intensity. *Nat. Commun.*, **7**, 10625, https://doi.org/10.1038/ncomms10625.

Leighton, H., S. Gopalakrishnan, J. A. Zhang, R. F. Rogers, Z. Zhang, and V. Tallapragada, 2018: Azimuthal distribution of deep convection, environmental factors, and tropical cyclone rapid intensification: A perspective from HWRF ensemble forecasts of Hurricane Edouard (2014). *J. Atmos. Sci.*, **75**, 275–295, https://doi.org/10.1175/JAS-D-17-0171.1.

Macdonald, N. J., 1968: The evidence for the existence of Rossby-like waves in the hurricane vortex. *Tellus*, **20**, 138–150, https://doi.org/10.3402/tellusa.v20i1.9993.

Montgomery, M. T., and R. J. Kallenbach, 1997: A theory for vortex Rossby-waves and its application to spiral bands and intensity changes in hurricanes. *Quart. J. Roy. Meteor. Soc.*, **123**, 435–465, https://doi.org/10.1002/qj.49712353810.

——, and R. K. Smith, 2014: Paradigms for tropical cyclone intensification. *Aust. Meteor. Oceanogr. J.*, **64**, 37–66, https://doi.org/10.22499/2.6401.005.

——, and ——, 2017: Recent developments in the fluid dynamics of tropical cyclones. *Annu. Rev. Fluid Mech.*, **49**, 541–574, https://doi.org/10.1146/annurev-fluid-010816-060022.

——, G. Kilroy, R. K. Smith, and N. Črnivec, 2020: Contribution of mean and eddy momentum processes to tropical cyclone intensification. *Quart. J. Roy. Meteor. Soc.*, **146**, 3101–3117, https://doi.org/10.1002/qj.3837.

Munsell, E. B., F. Zhang, J. A. Sippel, S. A. Braun, and Y. Weng, 2017: Dynamics and predictability of intensification of Hurricane Edouard (2014). *J. Atmos. Sci.*, **74**, 573–595, https://doi.org/10.1175/JAS-D-16-0018.1.

National Oceanic and Atmospheric Administration, 2017: National Hurricane Center Forecast Verification. NOAA, accessed 26 June 2019, https://www.nhc.noaa.gov/verification/verify5.shtml.

Nguyen, M. C., M. J. Reeder, N. E. Davidson, R. K. Smith, and M. T. Montgomery, 2011: Inner-core vacillation cycles during the intensification of Hurricane Katrina. *Quart. J. Roy. Meteor. Soc.*, **137**, 829–844, https://doi.org/10.1002/qj.823.

Nguyen, V. S., R. K. Smith, and M. T. Montgomery, 2008: Tropical-cyclone intensification and predictability in three dimension. *Quart. J. Roy. Meteor. Soc.*, **134**, 563–582, https://doi.org/10.1002/qj.235.

Ooyama, K., 1969: Numerical simulation of the life cycle of tropical cyclones. *J. Atmos. Sci.*, **26**, 3–40, https://doi.org/10.1175/1520-0469(1969)026<0003:NSOTLC>2.0.CO;2.

Persing, J., M. T. Montgomery, J. C. McWilliams, and R. K. Smith, 2013: Asymmetric and axisymmetric dynamics of tropical cyclones. *Atmos. Chem. Phys.*, **13**, 12 299–12 341, https://doi.org/10.5194/acp-13-12299-2013.

Powell, M. D., P. J. Vickery, and T. A. Reinhold, 2003: Reduced drag coefficient for high wind speeds in tropical cyclones. *Nature*, **422**, 279–283, https://doi.org/10.1038/nature01481.

Qiu, X., and Z.-M. Tan, 2013: The roles of asymmetric inflow forcing induced by outer rainbands in tropical cyclone secondary eyewall formation. *J. Atmos. Sci.*, **70**, 953–974, https://doi.org/10.1175/JAS-D-12-084.1.

Reasor, P. D., M. T. Montgomery, F. D. Marks, and J. F. Gamache, 2000: Low-wavenumber structure and evolution of the hurricane inner core observed by airborne dual-Doppler radar. *Mon. Wea. Rev.*, **128**, 1653–1680, https://doi.org/10.1175/1520-0493(2000)128<1653:LWSAEO>2.0.CO;2.

——, M. D. Eastin, and J. F. Gamache, 2009: Rapidly intensifying Hurricane Guillermo (1997). Part I: Low-wavenumber structure and evolution. *Mon. Wea. Rev.*, **137**, 603–631, https://doi.org/10.1175/2008MWR2487.1.

Reif, M., M. J. Reeder, and M. C. N. Hankinson, 2014: Vacillation cycles in WRF simulations of Hurricane Katrina. *Aust. Meteor. Oceanogr. J.*, **64**, 123–131, https://doi.org/10.22499/2.6402.004.

Rogers, R. F., P. D. Reasor, and S. Lorsolo, 2013: Airborne Doppler observations of the inner-core structural differences between intensifying and steady-state tropical cyclones. *Mon. Wea. Rev.*, **141**, 2970–2991, https://doi.org/10.1175/MWR-D-12-00357.1.

Rozoff, C. M., W. H. Schubert, and B. D. McNoldy, 2006: Rapid filamentation zones in intense tropical cyclones. *J. Atmos. Sci.*, **63**, 325–340, https://doi.org/10.1175/JAS3595.1.

——, J. P. Kossin, W. H. Schubert, and P. J. Mulero, 2009: Internal control of hurricane intensity variability: The dual nature of potential vorticity mixing. *J. Atmos. Sci.*, **66**, 133–147, https://doi.org/10.1175/2008JAS2717.1.

Schubert, W. H., M. T. Montgomery, R. K. Taft, T. A. Guinn, S. R. Fulton, J. P. Kossin, and J. P. Edwards, 1999: Polygonal eyewalls, asymmetric eye contraction, and potential vorticity mixing in hurricanes. *J. Atmos. Sci.*, **56**, 1197–1223, https://doi.org/10.1175/1520-0469(1999)056<1197:PEAECA>2.0.CO;2.

Short, C. J., and J. Petch, 2018: How well can the Met Office Unified Model forecast tropical cyclones in the western North Pacific? *Wea. Forecasting*, **33**, 185–201, https://doi.org/10.1175/WAF-D-17-0069.1.

Shu, S., J. Ming, and P. Chi, 2012: Large-scale characteristics and probability of rapidly intensifying tropical cyclones in the western North Pacific basin. *Wea. Forecasting*, **27**, 411–423, https://doi.org/10.1175/WAF-D-11-00042.1.

Sippel, J. A., and F. Zhang, 2008: A probabilistic analysis of the dynamics and predictability of tropical cyclogenesis. *J. Atmos. Sci.*, **65**, 3440–3459, https://doi.org/10.1175/2008JAS2597.1.

——, and ——, 2010: Factors affecting the predictability of Hurricane Humberto (2007). *J. Atmos. Sci.*, **67**, 1759–1778, https://doi.org/10.1175/2010JAS3172.1.

Sitkowski, M., J. P. Kossin, and C. M. Rozoff, 2011: Intensity and structure changes during hurricane eyewall replacement cycles. *Mon. Wea. Rev.*, **139**, 3829–3847, https://doi.org/10.1175/MWR-D-11-00034.1.

Smith, R. K., and M. T. Montgomery, 2015: Toward clarity on understanding tropical cyclone intensification. *J. Atmos. Sci.*, **72**, 3020–3031, https://doi.org/10.1175/JAS-D-15-0017.1.

——, J. A. Zhang, and M. T. Montgomery, 2017: The dynamics of intensification in a Hurricane Weather Research and Forecasting simulation of Hurricane Earl (2010). *Quart. J. Roy. Meteor. Soc.*, **143**, 293–308, https://doi.org/10.1002/qj.2922.

Sun, Y. Q., Y. Jiang, B. Tan, and F. Zhang, 2013: The governing dynamics of the secondary eyewall formation of Typhoon Sinlaku (2008). *J. Atmos. Sci.*, **70**, 3818–3837, https://doi.org/10.1175/JAS-D-13-044.1.

Tao, D., and F. Zhang, 2014: Effect of environmental shear, sea-surface temperature, and ambient moisture on the formation and predictability of tropical cyclones: An ensemble-mean perspective. *J. Adv. Model. Earth Syst.*, **6**, 384–404, https://doi.org/10.1002/2014MS000314.

——, and ——, 2015: Effects of vertical wind shear on the predictability of tropical cyclones: Practical versus intrinsic limit. *J. Adv. Model. Earth Syst.*, **7**, 1534–1553, https://doi.org/10.1002/2015MS000474.

Torn, R. D., 2016: Evaluation of atmosphere and ocean initial condition uncertainty and stochastic exchange coefficients on ensemble tropical cyclone intensity forecasts. *Mon. Wea. Rev.*, **144**, 3487–3506, https://doi.org/10.1175/MWR-D-16-0108.1.

Walters, D., and Coauthors, 2017: The Met Office unified model global Atmosphere 6.0/6.1 and JULES global land 6.0/6.1 configurations. *Geosci. Model Dev.*, **10**, 1487–1520, https://doi.org/10.5194/gmd-10-1487-2017.

Wang, B., and X. Zhou, 2008: Climate variation and prediction of rapid intensification in tropical cyclones in the western North Pacific. *Meteor. Atmos. Phys.*, **99**, 1–16, https://doi.org/10.1007/s00703-006-0238-z.

Wang, H., C.-C. Wu, and Y. Wang, 2016: Secondary eyewall formation in an idealized tropical cyclone simulation: Balanced and unbalanced dynamics. *J. Atmos. Sci.*, **73**, 3911–3930, https://doi.org/10.1175/JAS-D-15-0146.1.

Weckwerth, T. M., 2000: The effect of small-scale moisture variability on thunderstorm initiation. *Mon. Wea. Rev.*, **128**, 4017–4030, https://doi.org/10.1175/1520-0493(2000)129<4017:TEOSSM>2.0.CO;2.

Willoughby, H. E., J. A. Clos, and M. G. Shoreibah, 1982: Concentric eye walls, secondary wind maxima, and the evolution of the hurricane vortex. *J. Atmos. Sci.*, **39**, 395–411, https://doi.org/10.1175/1520-0469(1982)039<0395:CEWSWM>2.0.CO;2.

Wood, N., and Coauthors, 2014: An inherently mass-conserving semi-implicit semi-Lagrangian discretization of the deep-atmosphere global non-hydrostatic equations. *Quart. J. Roy. Meteor. Soc.*, **140**, 1505–1520, https://doi.org/10.1002/qj.2235.

World Meteorological Organization, 2017: Report on TC's key activities and main events in the region, 2016. WMO, 5 pp.

Ying, Y., and F. Zhang, 2017: Practical and intrinsic predictability of multiscale weather and convectively coupled equatorial waves during the active phase of an MJO. *J. Atmos. Sci.*, **74**, 3771–3785, https://doi.org/10.1175/JAS-D-17-0157.1.

Zhang, D.-L., and E. Altshuler, 1999: The effects of dissipative heating on hurricane intensity. *Mon. Wea. Rev.*, **127**, 3032–3038, https://doi.org/10.1175/1520-0493(1999)127<3032:TEODHO>2.0.CO;2.

——, Y. Liu, and M. K. Yau, 2001: A multiscale numerical study of Hurricane Andrew (1992). Part IV: Unbalanced flows. *Mon. Wea. Rev.*, **129**, 92–107, https://doi.org/10.1175/1520-0493(2001)129<0092:AMNSOH>2.0.CO;2.

Zhang, F., and J. A. Sippel, 2009: Effects of moist convection on hurricane predictability. *J. Atmos. Sci.*, **66**, 1944–1961, https://doi.org/10.1175/2009JAS2824.1.

——, and D. Tao, 2013: Effects of vertical wind shear on the predictability of tropical cyclones. *J. Atmos. Sci.*, **70**, 975–983, https://doi.org/10.1175/JAS-D-12-0133.1.

Zhang, J. A., R. F. Rogers, D. S. Nolan, and F. D. Marks, 2011: On the characteristic height scales of the hurricane boundary layer. *Mon. Wea. Rev.*, **139**, 2523–2535, https://doi.org/10.1175/MWR-D-10-05017.1.

Zhu, H., and R. K. Smith, 2020: A case study of a tropical low over northern Australia. *Quart. J. Roy. Meteor. Soc.*, **146**, 1702–1718, https://doi.org/10.1002/qj.3762.

Zhu, Z., and P. Zhu, 2014: The role of outer rainband convection in governing the eyewall replacement cycle in numerical simulations of tropical cyclones. *J. Geophys. Res. Atmos.*, **119**, 8049–8072, https://doi.org/10.1002/2014JD021899.